

New Anticancer Agents Mimicking Protein Recognition Motifs

Marco Persico,^{†,||} Anna Ramunno,^{*,‡} Vita Maglio,[‡] Silvia Franceschelli,^{*,‡} Chiara Esposito,[‡] Alfonso Carotenuto,^{†,||} Diego Brancaccio,[†] Valeria De Pasquale,[§] Luigi Michele Pavone,[§] Michela Varra,[†] Nausicaa Orteca,[†] Ettore Novellino,[†] and Caterina Fattorusso^{*,†}

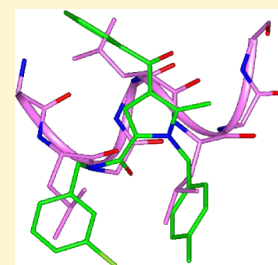
[†]Dipartimento di Farmacia, Università di Napoli "Federico II", Via D. Montesano 49, 80131 Napoli, Italy

[‡]Dipartimento di Farmacia, Università di Salerno, Via Giovanni Paolo II 132, 84084 Fisciano (SA), Italy

[§]Dipartimento di Medicina Molecolare e Biotecnologie Mediche, Università di Napoli "Federico II", Via S. Pansini 5, 80131 Napoli, Italy

Supporting Information

ABSTRACT: The novel tetrasubstituted pyrrole derivatives **8g**, **8h**, and **8i** showed selective cytotoxicity against M14 melanoma cells at low micromolar concentration. Structure–activity relationships (SARs) indicated the presence of three aromatic substituents on the pyrrole core as necessary for biological activity. Computational studies strongly suggest that the peculiar 3D orientation of these substituents is able to reproduce the hydrophobic side chains in LxxLL-like protein recognition motifs. Biological results showed altered p53 expression and nuclear translocation in cells sensitive to the compounds, suggesting p53 involvement in their anticancer mechanism of action. Unfortunately, because of poor solubility of the active analogues, it was not possible to perform further investigation by NMR techniques. Pharmacophore models were generated and used to perform 3D searches in molecular databases. Results indicated that two compounds share the same pharmacological profile and the same pharmacophoric features with our new derivatives, and one of them inhibited MDM2–MDM4 heterodimer formation.



■ INTRODUCTION

The identification of small molecules able to modulate specific intra- and intermolecular protein–protein interactions is necessary to clarify the dynamics of many cellular processes and promote the development of novel therapeutic approaches especially in the case of multifactorial diseases such as cancer.¹ Cancer cells are indeed characterized by the modification of one or more molecular pathways involved in the regulation of the cell life cycle. Thus, in this field many protein–protein interactions are promising druggable targets, such as those involving transcription factors and their regulators (e.g., p53, MDM2), microtubules, and proapoptotic and apoptotic proteins (e.g., Bcl-xl, Bcl2, Bax, Bid, XIAP).^{2,3}

The binding domains implicated in protein–protein interactions can be small binding clefts or large surfaces and generally include smaller regions, called hot spots,⁴ which represent energetic focal points on protein surfaces that are major contributors to the binding energy of the complex. These highly conserved binding subregions have a functional and structural adaptivity and typically are able to accommodate small organic compounds based on different scaffolds.⁵ It is noteworthy that the same (or homologous) hot spot can adapt the same (or homologous) residues in different structural contexts. For example, the same MDM2-binding domain can be recognized by p53, as well as by its homologous proteins p63 and p73 and potentially by many other proteins containing similar binding motifs, whose biological relevance is, in some cases, still not clarified.⁶ On the other hand, recognition motifs, such as polyproline and LxxLL-like motifs, can bind to different protein domains.⁷ Consequently, a small molecular scaffold able to

mimic protein recognition motifs is potentially able to alter different protein–protein interactions of a given molecular pathway.

Understanding the structural basis for peptidomimetic inhibition holds the key to developing novel, highly effective, and selective drug candidates. As an example, we previously reported that the particular spatial orientation of the three aromatic rings of paclitaxel is able to mimic the hydrophobic side chains of the interacting residues of SH3 domains, thus accounting for its activity toward multiple protein targets involved in cellular apoptosis.⁸

On these bases, in the search for new anticancer leads, we synthesized a small set of tetrasubstituted pyrrole derivatives with the aim of developing stable mimics of LxxLL-like motifs, which have been reported as one of the most representative protein-recognition motifs in cell cycle regulation.⁷ Two series of compounds were synthesized, namely, (a) 4-acetyl derivatives (**8a–d**, Table 1) and (b) 4-benzoyl derivatives (**8e–n**, Table 1), and their antiproliferative activity was evaluated against different cancer cell lines (MCF7, Huh7, M14, Jurkat), as well as on mouse monocyte macrophages (Raw 264-7) cell line, by means of the MTT assay. Three of them, **8g–i**, showed a selective cytotoxicity against M14 melanoma cells at low micromolar concentration. Then active derivatives **8g–i** were further investigated for their mechanisms of action by means of biological, NMR, and molecular modeling studies.

Received: March 20, 2013

Published: July 23, 2013

Table 1. Physical and Chemical Data for Compounds 8a–n

8a–n

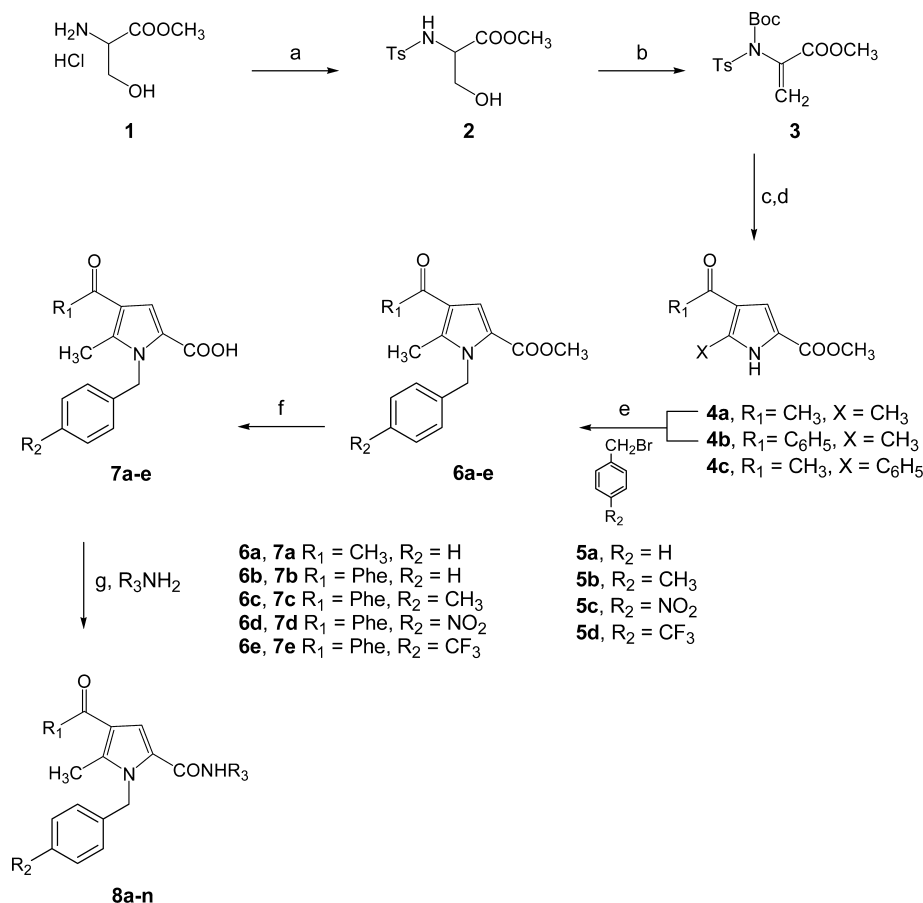
Compd	R ₁	R ₂	R ₃	Yield ^a	mp (°C) ^b	Formula	Anal. ^c
8a	CH ₃	H		85	133-135	C ₂₂ H ₂₂ N ₂ O ₂	C, H, N
8b	CH ₃	H		94	184-186	C ₂₁ H ₂₆ N ₂ O ₂	C, H, N
8c	CH ₃	H		92	94-96	C ₂₄ H ₂₆ N ₂ O ₂	C, H, N
8d	CH ₃	H		91	130-132	C ₂₂ H ₂₁ IN ₂ O ₂	C, H, N
8e		H		82	116-118	C ₂₇ H ₂₄ N ₂ O ₂	C, H, N
8f		H		89	156-158	C ₂₆ H ₂₈ N ₂ O ₂	C, H, N
8g		H		87	127-129	C ₂₇ H ₂₃ IN ₂ O ₂	C, H, N
8h		H		90	118-120	C ₂₇ H ₂₃ ClN ₂ O ₂	C, H, N
8i		CH ₃		84	141-143	C ₂₈ H ₂₅ ClN ₂ O ₂	C, H, N
8j		NO ₂		72	129-130	C ₂₇ H ₂₂ ClN ₃ O ₄	C, H, N
8k		CF ₃		87	123-124	C ₂₈ H ₂₂ ClF ₃ N ₂ O ₂	C, H, N
8l		H		85	126-127	C ₂₇ H ₂₃ N ₃ O ₄	C, H, N
8m		H		91	142-144	C ₂₉ H ₂₈ N ₂ O ₄	C, H, N
8n		H		77	125-126	C ₃₂ H ₂₆ N ₂ O ₂	C, H, N

^aYields refer to isolated and purified materials. ^bRecrystallization solvent: EtOAc/*n*-hexane. ^cAll the compounds were analyzed within $\pm 0.4\%$ of the theoretical values.

RESULTS AND DISCUSSION

Chemistry. We used a synthetic approach that enabled us to easily introduce (1) three lipophilic groups with

different size and substituents in 1,2,4-positions of the pyrrole core and (2) one hydrogen bond donor (NH) and two hydrogen bonds acceptors (C=O) in 2 and 4 positions.

Scheme 1^a

^aReagents and conditions: (a) tosyl chloride, TEA, DCM, 0 °C to rt, overnight; (b) (Boc)₂O, DMAP, AcCN, rt; (c) Cs₂CO₃, dry AcCN, pentane-2,4-dione for **4a**, and 1-phenyl-1,3-butanedione for **4b** and **4c**; (d) THF, DCM, rt; (e) 50% w/v NaOH, TBAH, DCM, 0 °C to rt, overnight; (f) 2 M NaOH, MeOH, reflux, 2 h; (g) HOBT, HBTU, NMM, DMF, rt.

The synthetic route of the title compounds **8a–n** is outlined in Scheme 1.

The 4-acetyl-2-methoxycarbonyl-5-methylpyrrole **4a** and its 4-benzoyl analogue **4b** were synthesized according to a slightly modified procedure previously reported by Ferreira et al.^{9,10} In detail, reaction of (±)-serine methyl ester hydrochloride **1** with *p*-toluenesulfonyl chloride afforded the derivative **2**,¹¹ which in turn was reacted with *tert*-butyl pyrocarbonate, (Boc)₂O, and a catalytic amount of 4-dimethylaminopyridine (DMAP) to give the dehydroalanine derivative **3**.

Then the intermediate **3** was reacted with pentane-2,4-dione, using 1 equiv of Cs₂CO₃ as base, and the crude mixture was treated with 10% THF in dichloromethane at room temperature to yield the pyrrole derivative **4a**. A similar procedure was performed with 1-phenyl-1,3-butanedione instead of pentane-2,4-dione to give a mixture of 4-benzoyl-5-methyl-1*H*-pyrrole-2-carboxylic acid methyl ester (**4b**) and its regioisomer 4-acetyl-5-phenyl-1*H*-pyrrole-2-carboxylic acid methyl ester (**4c**), not previously described, in an approximately 4:1 ratio. The structures of **4b** and **4c** were confirmed by the analysis of the ROESY spectra. In particular, a ROE signal between pyrrole NH and C5-methyl was observed only in the spectrum of compound **4b** (Figure 1S1 in Supporting Information). For compound **4c**, a diagnostic ROE signal was observed between pyrrole NH and H1'/H5' of the phenyl ring (Figure 2S1). The intramolecular distances associated with these two diagnostic ROE signals were evaluated

by integration of the ROESY spectra to be 3.20 and 3.30 Å, respectively. These values are in good accordance with distances present in experimentally determined structures containing the 2-methyl-1*H*-pyrrole and the 2-phenyl-1*H*-pyrrole fragments, i.e., 3.10 and 3.45 Å, respectively (Cambridge Structural Database (CSD) codes POPPAM and IDOCUZ). Our ¹H and ¹³C NMR data (see Experimental Section) of the regioisomer **4b** do not match those reported by Ferreira et al.⁹ for the same compound. Actually, ¹H and ¹³C NMR spectra of the isomer **4c** are comparable to those reported by Ferreira et al. Hence, we argue that there was a misassignment in that case. Indeed, our ¹H NMR spectrum of **4b** matches that described by Toplak et al. who employed a different synthetic approach.¹²

N-Benzylation of pyrrole derivatives **4a,b** with commercially available benzyl bromides **5a–d** afforded the esters **6a–e**, which in turn were hydrolyzed with 2 M NaOH at room temperature. The corresponding acids **7a–e** were precipitated by adding 2 M HCl and were subjected to a coupling reaction with an appropriate amine using 1-hydroxybenzotriazole (HOBT) and *O*-benzotriazol-1-yl-*N,N,N',N'*-tetramethyluronium hexafluorophosphate (HBTU) as coupling reagents in the presence of diisopropylethylamine (DIPEA) in DMF to provide the final compounds **8a–n** (Table 1) in good yields.

Cytostatic Effect of 8g–i Derivatives. To evaluate the inhibitory effect of **8a–n** derivatives, we used concentrations ranging from 100 nM to 100 μM in the culture media of different

human tumor cell lines (M14, Huh7, MCF7, Jurkat) and on a mouse monocyte macrophages (Raw 264-7) cell line. Cells were treated for 24 and 48 h, and the cell viability was measured by the MTT assay. Compounds **8g–i** showed antiproliferative activity on a single cell line, M14, and results are summarized in Table 2.

Table 2. Antiproliferative Activity of Compounds **8g–i: IC₅₀ Measured against Cancer (M14, MCF7, Huh7, and Jurkat) and Normal (Raw 264-7) Cell Lines after 48 h of Treatment**

compd	IC ₅₀ (μM)				
	M14 ^a	MCF7 ^b	Huh7 ^c	Jurkat ^d	Raw 264-7 ^e
8g	5.0 ± 0.1	>100	>100	>100	>100
8h	7.5 ± 0.1	>100	>100	>100	>100
8i	2.5 ± 0.1	>100	>100	>100	>100

^aHuman melanoma cell line. ^bHuman breast cancer cell line. ^cHuman hepatocarcinoma cell line. ^dImmortalized line of T lymphocyte cells. ^eCell line murine macrophage.

The IC₅₀ concentrations of compounds were used in all subsequent experiments.

The selective cytotoxicity at tested concentrations of **8g–i** toward M14 cell line suggests a mechanism of action based on the interaction with a molecular pathway which is altered in this cancer cells.

To characterize the inhibitory effect, we determined growth rates of M14 cells in the absence or presence of active compounds **8g–i** by the trypan blue dye exclusion method.¹³ Since we did not observe a significant increase in cell death (trypan blue positive) in treated cells compared with control cells, we can conclude that proliferation of exponentially growing cells was inhibited by treatment with an inhibitory effect seen after 24 h, suggesting that these compounds have a cytostatic effect.

Two sets of M14 cells were treated with **8g–i** for 24 h. The medium was then removed, and cells were resuspended in a compound-free medium. The cells were incubated for further 24 and 48 h and analyzed by MTT assay to assess cell viability.

The obtained data suggest that incubation of the cells in compound-free medium for 48 h was sufficient to restore normal cell proliferation (data not shown). The reversible effect on cell proliferation indicates a specificity of action of the compounds and lack of toxicity once removed from the cells after 24 h of incubation.

Effect on Cell Cycle Progression and Apoptosis Analyses. On the basis of the results obtained, we characterized the cytostatic effect by performing distribution analysis by flow cytometry during the different cell cycle phases.

As shown in Figure 1 (panel A), all three tested compounds **8g–i** induced accumulation of cells in S phase and a corresponding decrease in G0/G1 and G2/M phases after a 24 h treatment. Moreover, cell cycle deregulation leading to apoptosis occurred after 48 h of treatment (Figure 1, panel B).

The S-phase arrest was confirmed by nucleus DAPI staining where we observed differences in the size of the nucleus of treated cells probably due to an increase in DNA content and inability of the cells to divide (Figure 2).

Cyclin A Expression and Involvement of p53. To understand the role of pyrrole derivatives **8g–i** on cell cycle arrest, we assessed their effect on cyclin A, a molecular marker associated with G1/S phase, by Western blotting (Figure 3).¹⁴

As reported in Figure 3, treatment of M14 cells with the active compounds **8g–i** led to an increase in the expression of cyclin A known to promote S-phase entry in mammals. Our data suggest that the tested compounds induce a block in the S phase of the cell cycle and are consistent with our results obtained by flow cytometry analysis. Interestingly, the increase is present at 24 h for all compounds and at 48 h for compounds **8g** and **8i** but not for **8h**, suggesting the presence of a different mechanism that needs to be further elucidated.

Since **8g–i** compounds reduce cell viability, induce cell cycle arrest, and affect cyclin A expression, we investigated the expression of p53 by Western blotting in M14 and Huh7 cells after 24 and 48 h of treatment (Figure 4).¹⁵ Huh7 cells were used as a control, since they also contain a missense mutation in p53 gene but they are not sensitive to **8g–i**.

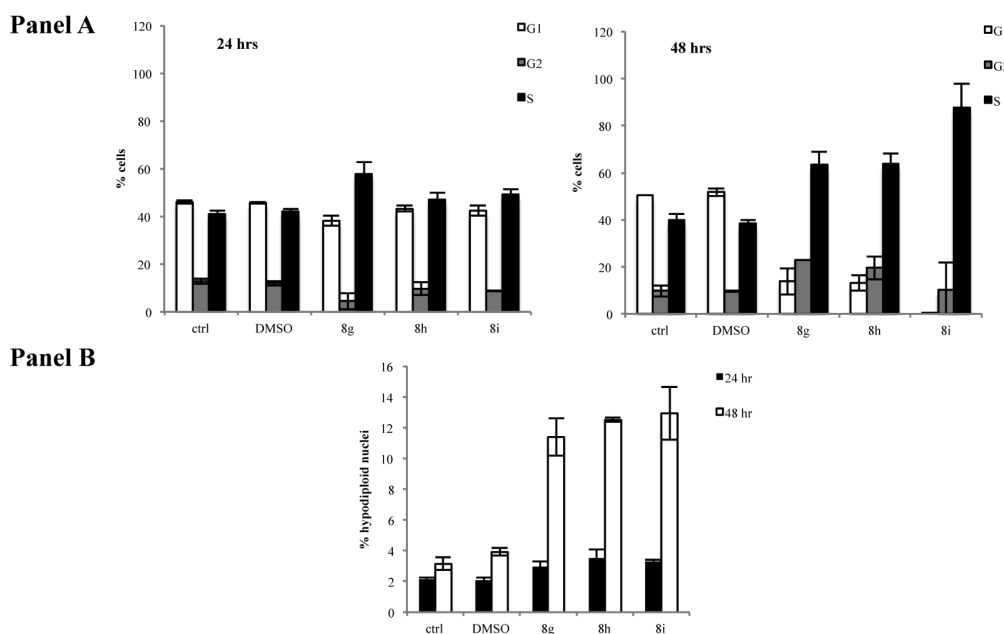


Figure 1. Cell cycle (A) and apoptosis profile (B) in M14 cell line in presence of **8g–i** derivatives after 24 and 48 h of treatment.

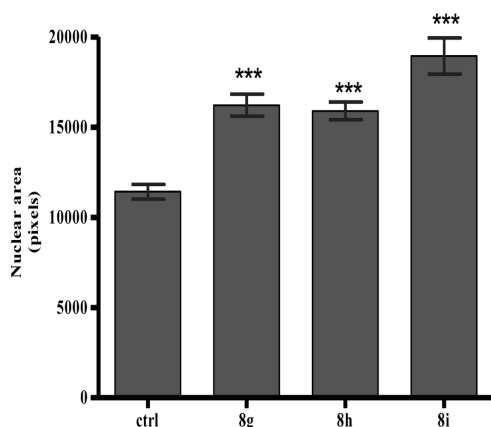


Figure 2. M14 cells were treated for 24 h with 8g-i derivatives, and nuclear areas were measured using ImageJ software after DAPI staining. Results are expressed as the mean \pm SEM of at least 20 independent measurements. *** denotes $P < 0.001$ vs control. Statistical significance was measured using one way ANOVA. The Bonferroni post test was used to compare differences between the groups. All measured values were significant according to statistical test ($P < 0.05$).

These compounds enhance p53 expression in M14 cells at 24 h (an effect that disappeared after 48 h of incubation) but not in Huh7 cells (Figure 4). Thus, the variation of p53 expression observed in M14 cell line is due to a specific effect of these compounds. The increase of p53 in M14 cells, sensitive to the compounds, might suggest that, although mutated, it could still have a role in the regulation of cell proliferation.

Furthermore, we examined whether treatment with 8g-i modified the nuclear translocation of p53. Accumulation of p53 in the nuclear fraction increased in cells treated for 24 h compared with control cells, an effect that disappeared after 48 h of incubation in accordance with the p53 expression results (Figure 5).

We focused our attention on p53 protein, since the critical role of this transcription factor in cell cycle control is well documented. In recent years the biological relevance of a specific p53 status (wild-type or mutated) has been evaluated in more detail for many cell lines. For example, it has been reported that some p53 mutants expressed in cell lines have a residual or a temperature-sensitive transcriptional activity;¹⁶ additionally, "gain of function" of some mutant p53 proteins and controversial p53 status in many cell lines have been recently described.¹⁷

To the best of our knowledge, only one mutation has been reported for the p53 protein in M14¹⁸ (G266E) and Huh7 (Y220C)¹⁹ cell lines. Furthermore, a recent study on a set of spiro(oxindole-3,3'-thiazolidine)-based derivatives tested on

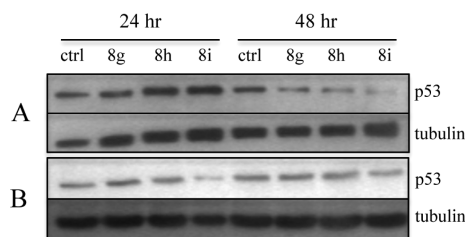


Figure 4. p53 expression in M14 (A) and Huh7 (B) cell line after 24 and 48 h of 8g-i derivatives treatment.

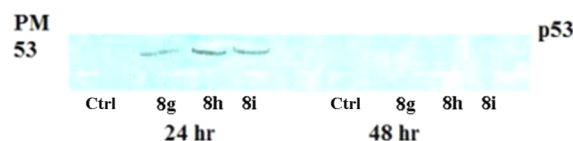


Figure 5. Nuclear p53 expression in M14 cells after 24 and 48 h of 8g-i treatment. Same amounts of nuclear lysate were loaded on 12% SDS-PAGE, blotted onto nitrocellulose membrane, and p53 antibody was used to visualize the p53 nuclear fraction.

M14 melanoma cell line found a potential inhibition of p53-MDM2 interaction on the basis of NMR studies.²⁰ Finally, increasing evidence supports a role for p53 and its major negative regulators, MDM2/MDM4, in melanogenesis without an exhaustive analysis of single melanoma cell line.²¹

NMR Analysis. The ability of compound 8i to block p53-MDM2 interaction was investigated by NMR analysis. Holak et al. have recently described a two-dimensional ¹⁵N-HSQC based NMR assay to determine the effect of antagonists on protein-protein interactions.^{22,23} The method, named AIDA (for antagonist induced dissociation assay), provides information on whether an antagonist of a protein-protein interaction is strong enough to dissociate the complex and whether its mode of action is modulated by denaturation, precipitation, or release of a protein in its functional folded state. AIDA requires the use of a large protein fragment (larger than 30 kDa) to bind to a small reporter protein (less than 20 kDa). In appropriate conditions (flexible residues), 1D proton NMR spectra may suffice for monitoring the states of proteins in complexes upon treatment with ligands. Because of the highly flexible nature of the N-terminal domain of p53, the p53-MDM2 complex is suitable for 1D proton NMR application. In particular, the ¹H^ε side chains of W23 and W53 produce sharp lines in the free p53 1D proton spectrum. When the complex with MDM2 is formed, the W23 signal disappears, since W23, together with the p53 residues 17–26, comprises the primary binding site for MDM2.

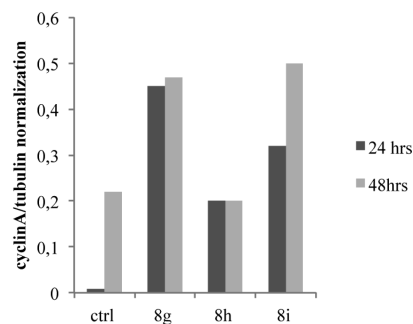
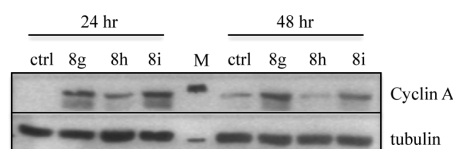


Figure 3. Western blotting (left) and histogram profile (right) of cyclin A expression after 24 and 48 h of 8g-i derivatives treatment at IC₅₀ concentration. Cyclin A up-regulation is required for induction and maintenance of cell cycle arrest.

Upon binding, these residues participate in well-defined structures of large p53–MDM2 complexes, whereas W53 is still not structured when p53 is bound to MDM2.^{22–24} The observed $1/T_2$ transverse relaxation rate of the bound W23 in the complexes increases significantly, and the broadening of NMR resonances results in the disappearance of this signal from the spectra.

Figure 6 shows the NMR spectrum of the tryptophan residues of the p53–MDM2 complex (0.1 mM); only W53 $^1\text{H}^\epsilon$ side

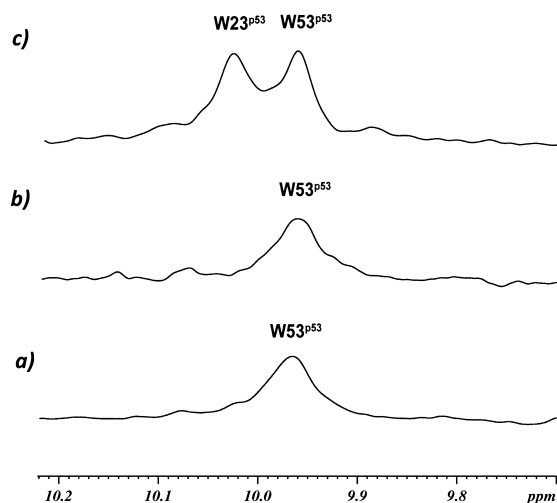


Figure 6. One-dimensional proton spectra of the side chains of tryptophans (W) of p53–MDM2 complex (a), after addition of **8i** (b), and nutlin-3 (c).

chains signal can be detected. The addition of **8i** from a stock DMSO solution (0.1 mM formal final concentration) to the p53–MDM2 complex caused sample precipitation. The full 1D ^1H NMR spectrum of the supernatant solution did not change compared to that acquired before **8i** addition, indicating that only **8i** precipitated after its addition. In particular, the W23 peak was still not observable (Figure 6b), indicating that the p53–MDM2 was not dissociated. Nutlin-3 was also used as positive control (Figure 6c). Its addition (0.1 mM) caused a complete p53 release.^{22,23}

Because of the observed precipitation of **8i**, the solubility of the compound was measured in the same buffer solution used for NMR experiments adopting the Lipinski et al. method.²⁵ The compound was dissolved in DMSO at 4.6 $\mu\text{g}/\mu\text{L}$ to obtain a 10 mM stock solution which was added to the phosphate buffer solution. Precipitation was quantified by measuring UV absorbance in the 500–900 nm range (Figure 3SI). The result is that the solubility of **8i** is $\leq 3.1 \mu\text{g}/\text{mL}$ ($\leq 6.8 \mu\text{M}$).

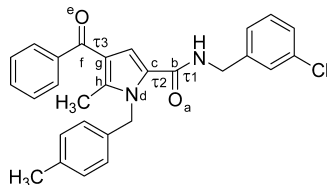
The high affinity of the MDM2–p53 complex ($K_D \approx 0.7 \mu\text{M}$)²⁶ along with the high concentration of the two proteins required for the NMR analysis (100 μM) allows the detection of only very soluble inhibitors.^{22,23} Thus, in the experimental conditions needed for NMR analysis, **8i** would not be able to displace p53 even if it was a high affinity ligand of MDM2.

Conformational Analysis and SAR Studies. A comprehensive conformational analysis was performed on the newly synthesized derivatives **8a–n** (Table 1). The conformational space was sampled by using a protocol including molecular dynamics (simulated annealing) and mechanic calculations followed by quantum mechanical (PM6) full geometry optimization (see Experimental Section). Obtained conformers were ranked by their conformational energy values and grouped

into families. For clarity of presentation, herein only results obtained for compound **8i** are reported (results obtained for **8e**, **8g**, **8h**, **8j**, **8k**, and **8l** are available in the Supporting Information).

First, low energy conformers, i.e., within 5 kcal/mol from the global minimum energy value ($\Delta E_{\text{GM}} \leq 5$), were classified into different conformational families, named TCC, CCC, TCT, TTC, and CCT according to the synperiplanar or antiperiplanar conformation of the torsion angles τ_1 , τ_2 , and τ_3 , and occurrence rates together with the range of ΔE_{GM} values were calculated for each family (Table 3 and Tables 1SI–6SI).

Table 3. ΔE_{GM} (kcal/mol), Torsional Angles (deg), and Occurrence Rates (%) of Conformational Families of **8i** Considering PM6 Conformers within 5 kcal/mol from the Global Minimum



family	ΔE_{GM}^a (kcal/mol)	torsional angle (deg)			occurrence rate (%)
		τ_1^b	τ_2^c	τ_3^d	
TCC	0.00–1.54	~180	~0.00	~0.00	35.0
CCC	1.57–2.95	~0.00	~0.00	~0.00	19.0
TCT	2.08–3.81	~180	~0.00	~180	25.0
TTC	2.46–3.85	~180	~180	~0.00	15.0
CCT	3.65–4.63	~0.00	~0.00	~180	6.00

^aThe values reported refer to the lowest and the highest energy conformers of the family. ^b τ_1 torsional angle is calculated considering the amide bond atoms. ^c τ_2 : a, b, c, and d atoms. ^d τ_3 : e, f, g, and h atoms.

Since the presence of three aromatic substituents on the pyrrole ring is necessary for biological activity, they were considered as pharmacophoric moieties, and their relative distances were calculated in all low energy conformers (Tables 4, 7SI, and 8SI; Figure 7). The result is that each conformational family is characterized by more than one set of intramolecular distances, according to the values of torsion angles τ_4 and τ_5 , giving rise to different subfamilies.

Active compounds **8g–i** showed a similar conformational behavior; moreover, since each set of intramolecular distances is univocally associated with one conformational subfamily, they also share the same orientation of the aromatic rings X, Y, and Z (Tables 4, 7SI, and 8SI). By consequence, the different potency shown by compounds **8g–i** (activity rank order **8i** > **8g** > **8h**, Table 2) is due to specific molecular interactions with the target established by (i) the para-substituent of the X ring (R_2 ; **8i** vs **8g** and **8h**, Table 1) and (ii) the meta-substituent of the Y ring (R_3 ; **8i** and **8h** vs **8g**, Table 1). Indeed, structure–activity relationships (SARs) indicate strict requirements for the substitution of the aromatic rings X and Y. The presence of a meta-halogen substituent on the Y ring (R_3) was crucial for biological activity (**8e** vs **8g** and **8h**, Tables 1 and 2), and its replacement with a nitro group led to an inactive compound (**8l**). On the other hand, the para-substitution of the X ring caused either an improvement or a loss of biological activity, depending on the nature of the R_2 substituent (**8i**, **8j**, and **8k** vs **8h**; Tables 1 and 2). To further investigate these SARs, the conformational

Table 4. Intramolecular Distances (Å), Torsional Angle (deg), and Occurrence Rates (%) of Conformational Subfamilies of **8i** Considering PM6 Conformers within 5 kcal/mol from the Energy Global Minimum

family	subfamily	distance (Å)			torsional angle ^a (deg)		occurrence rate (%)
		d_1 (X–Y)	d_2 (X–Z)	d_3 (Y–Z)	τ_4 ^b	τ_5 ^c	
TCC	I	5.7	9.0	9.1	~90	~-100	20.0
	II	8.8	9.0	8.0	~90	~90	15.0
CCC	I	5.6	9.0	8.6	~85	~100	10.0
	II	8.4	8.9	4.6	~85	~-95	6.00
	III	4.8	8.5	5.6	~80	~60	1.00
	IV	7.9	8.7	8.4	~105	~-70	2.00
TCT	I	6.1	8.1	11.2	~90	~-90	12.5
	II	8.8	7.0	11.1	~105	~90	12.5
TTC	I	4.6	9.2	10.7	~85	~-100	14.0
	II	6.3	9.2	8.9	~90	~90	1.00
CCT	I	5.7	8.3	10.6	~85	~100	5.00
	II	7.9	6.9	9.4	~105	~-80	1.00

^aConformational enantiomers present the same absolute values of torsional angles, with τ_4 and τ_5 having the opposite sign. ^b τ_4 : c, d, i, and j atoms. ^c τ_5 : b, k, l, and m atoms.

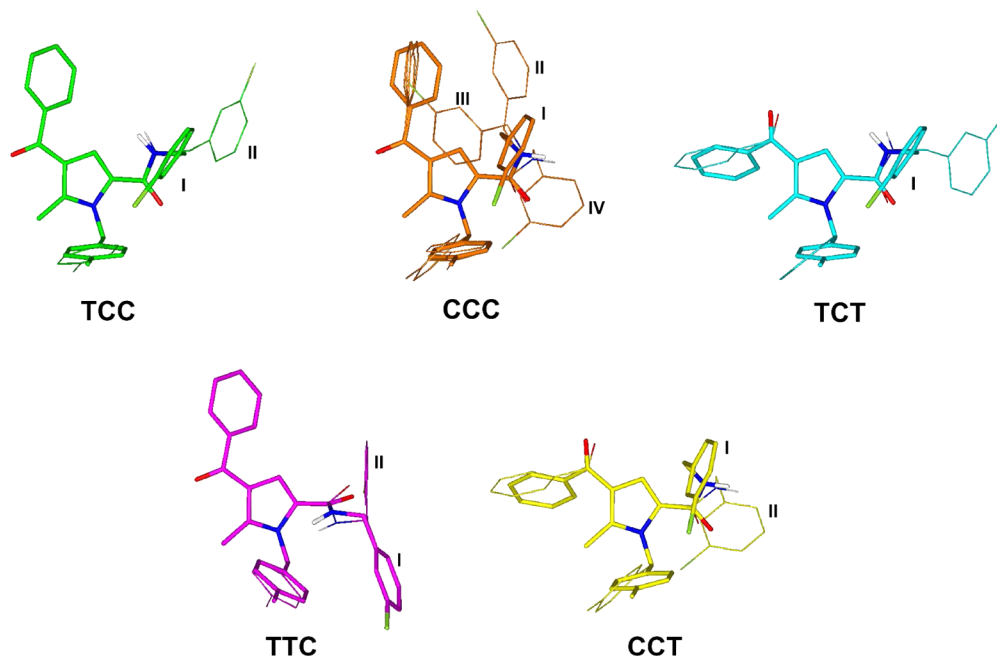


Figure 7. Molecular models of **8i** conformational families, classified as in Table 4. The lowest energy conformer of each family is displayed as sticks. Conformers belonging to other subfamilies are superimposed by pyrrole ring atoms and displayed as lines. Heteroatoms are colored by atom type: O, red; N, blue; S, yellow; Cl, light green. Hydrogens are omitted for clarity with the exception of that bonded to the amide nitrogen.

features of active analogues **8g–i** were compared to those of inactive analogues **8e** (Table 1SI) and **8j–l** (Table 4SI–6SI). The result is that for all compounds the three most populated conformational families are TCC, CCC, and TCT, with the following rank order: TCC > TCT > CCC. Significant differences in the conformational behavior of active vs inactive compounds can only be found in the rate of TTC conformers, although not in all cases. In detail, the unsubstituted analogue **8e** shows a decrease of TTC conformers (1%) and an increase of TCC conformers (43%) with respect to active compounds **8g–i**,

whereas the replacement of the chlorine atom at R₃ (**8i**) with a nitro group (**8l**) does not alter the conformational preference of the resulting structure (Table 4 vs Table 6SI). By consequence, it is likely that the inactivity of **8l** is due to unfavorable steric interactions with the target caused by the greater size of the nitro group with respect to the chlorine atom of **8i**. Also, compound **8k**, which has a trifluoromethyl substituent at R₂ instead of the methyl of **8i** (Table 1), showed a conformational behavior comparable to that of **8i**, with only a slight increase of TCC and a slight decrease of CCC conformational families

Table 5. Distances between the Centroids of the Side Chains of Interacting Residues in LxxLL-like Motifs

motif	PDB code	distance (Å)					
		$i, i + 3$	$i, i + 4$	$i, i + 7$	$i + 3, i + 4$	$i + 3, i + 7$	$i + 4, i + 7$
$^{345}\text{LxxLL}^{349}$	2J7X ^a	7.9	5.0		8.6		
$^{19}\text{FxxLWxxL}^{26}$	1YCR ^b	7.8	5.3	8.2	10.2	9.7	4.3

^aNuclear receptor coactivator 5. ^bp53.

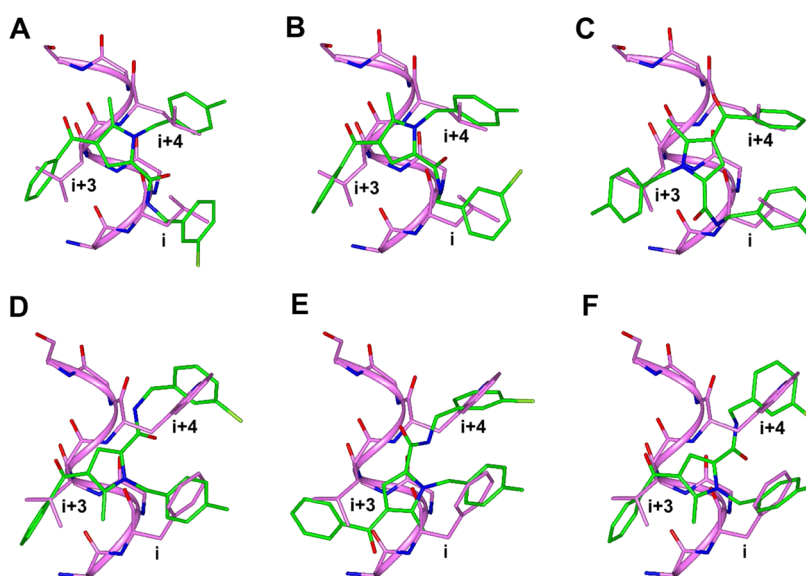


Figure 8. Superimposition of TCC I (A), CCC I (B), CCC II (C), TCT I (D), TTC I (E), and CCT I (F) lowest energy conformers of **8i** (carbons in green) on the $i, i + 3, i + 4$ residues both of $^{345}\text{LxxLL}^{349}$ (A, B, C) motif present in the 2J7X structure (carbons in pink) and $^{19}\text{FxxLWxxL}^{26}$ (D, E, F) motif present in 1YCR structure (carbons in pink). Overlaying amino acid position is indicated. The motif backbone and interacting amino acids are displayed as stick. Heteroatoms are colored by atom type: O, red; N, blue; Cl, light green. Hydrogens are omitted for clarity.

(Table 4 vs Table 5SI). Since the trifluoromethyl of **8k** and the methyl group of **8i** share similar steric parameters, then the strong electronegativity of the CF_3 substituent is responsible for the activity decay of **8k**. Accordingly, the inactive compound **8j** is also characterized by the presence of an electron-withdrawing group at R_2 (Table 1); however, in the case of **8j**, an increase of TCT conformational family (35%, Table 4SI) and the absence of TTC conformers are observed too.

Finally, inactive analogues **8m** and **8n**, both characterized by the presence of a bulky substituent at the ortho position on ring Y (Table 1), presented different electronic, steric, and conformational features compared to active **8g–i** (data not shown).

Structural Comparison with LxxLL-like Motifs. In order to evaluate the peptidomimetic ability of our active analogues, a structural analysis was performed on the X-ray structures of LxxLL-like motifs involved in protein–protein interactions, such as (i) p53 in complex with HDM2 protein (PDB code 1YCR) and (ii) nuclear receptor coactivator 5 in complex with the estrogen receptor β (PDB code 2J7X). Motif residues responsible for protein–protein interactions were identified, and the distances between the centroids of the interacting side chains were calculated (Table 5).

Intramolecular distances reported in Table 5 were crossed with those of **8g–i** (Tables 4, 7SI, and 8SI). Conformational subfamilies matching the specified similarity criteria were selected (see Experimental Section for details). Low energy PM6 conformers belonging to the selected conformational subfamilies were superimposed on the $^{345}\text{LxxLL}^{349}$ and/or $^{19}\text{FxxLWxxL}^{26}$ motif by fitting the centroids of the aromatic rings X, Y, and Z on the centroids of the side chains of the corresponding residues.

It emerged that some conformational subfamilies of **8g–i** are able to reproduce the orientation of $i, i + 3, i + 4$ residues of LxxLL-like motifs, like those present in p53 (i.e., CCC I–II, TCT I, TTC I, CCT I) and in nuclear receptor coactivator 5 (i.e., TCC I, CCC I–II) (Figure 8 and Figure 4SI).

On the other hand, conformational subfamilies TCC II, CCC IV, TCT II, TTC II, and CCT II are able to mimic the $i, i + 3, i + 7$ residues of the $^{19}\text{FxxLWxxL}^{26}$ motif present in 1YCR (Figure 9A–E).

Thus, just from rotation of rings X and Y, i.e., from variation of τ_4 and τ_5 (Table 4, Figure 7), **8g–i** are able to mimic the $i, i + 3$, and $i + 4$, as well as the $i, i + 3$, and $i + 7$ residues of LxxLL-like motifs. Nevertheless, only CCC III conformers are able to reproduce the orientation of the hydrophobic side chains of $i, i + 4, i + 7$ residues (Figure 9 F), which represent the key interacting residues of the p53 $^{19}\text{FxxLWxxL}^{26}$ binding motifs in its interaction with MDM2.

It is noteworthy that apart from the superimposition of the hydrophobic moieties, the overall shape of the molecule and the positioning of the heteroatoms (including the direction of some carbonyl functions) of the active analogues **8g–i** reproduce those of the motif interacting residues.

Interestingly, because of the pseudosymmetry of the $^{19}\text{FxxLWxxL}^{26}$ motif, some **8g–i** conformational enantiomers are able to reproduce this functional motif by fitting specular residues (Figure 5SI).

Pharmacophore Generation and 3D Database Searching. To further investigate the molecular mechanism of action of the new derivatives, pharmacophore models were generated and used to perform 3D searches in molecular databases.

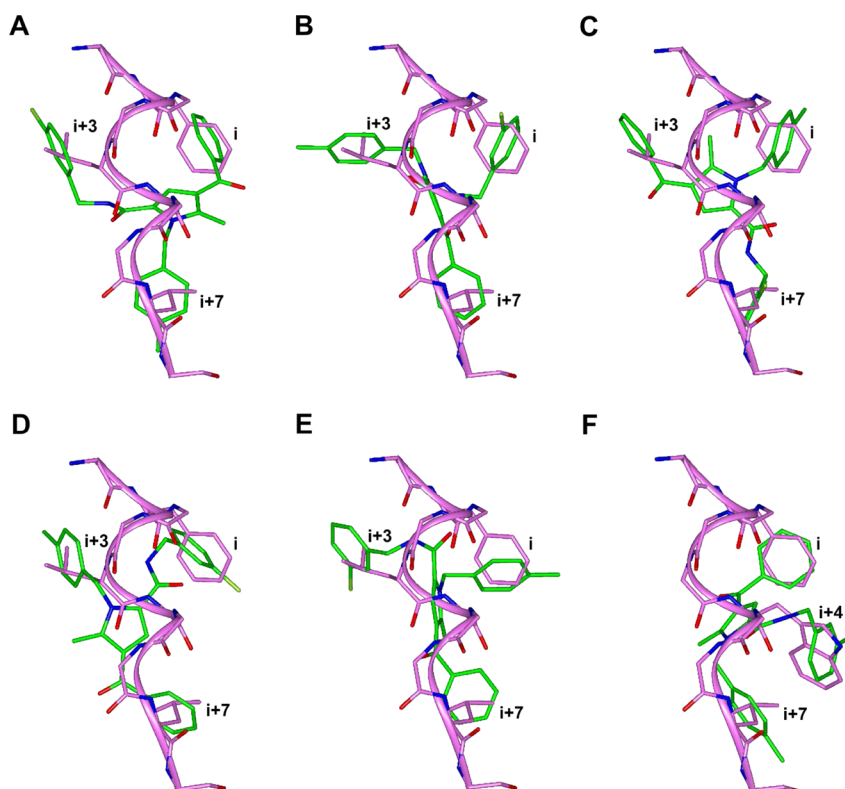


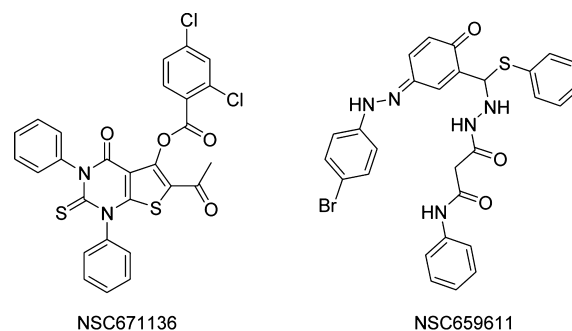
Figure 9. Superimposition of TCC II (A), CCC IV (B), TCT II (C), TTC II (D), and CCT II (E) lowest energy conformers of **8i** (carbons in green) on the i , $i+3$, $i+7$ residues of $^{19}\text{FxxLWxxL}^{26}$ motif in the 1YCR structure (carbons in pink) and of CCC III (F) conformer of **8i** (carbons in green) on the i , $i+4$, $i+7$ residues of $^{19}\text{FxxLWxxL}^{26}$ motif in the 1YCR structure (carbons in pink). Overlaying amino acid position is indicated. The motif backbone and interacting amino acids are displayed as stick. Heteroatoms are colored as follows: O, red; N, blue; Cl, light green. Hydrogens are omitted for the sake of clarity.

A pharmacophore model was produced for each conformational subfamily of **8g–i**, i.e., for each set of pharmacophoric distances (Table 9SI) (Catalyst Software; see Experimental Section for details). The three phenyl rings and the halogen atom on ring Y were selected as pharmacophore fragments. The generated pharmacophore models were then employed to perform as many 3D database searches in molecular databases (see Experimental Section). The resulting 1529 hits were analyzed and filtered on the basis of the compatibility of their reported biological activity with the activity profile of our active analogues (PubChem BioAssay database;²⁷ www.ncbi.nlm.nih.gov/pcassay). First, only compounds whose biological activity on M14 cells has been explored were taken into consideration. This reduced the number of hits to 189. Among them, only 19 were reported to be active in the micromolar range ($<10\ \mu\text{M}$) on M14 cells. Two of them (Chart 1), NSC671136 (CID 383092, pubchem.ncbi.nlm.nih.gov/summary/summary.cgi?cid=383092) and NSC659611 (CID 6712209, pubchem.ncbi.nlm.nih.gov/summary/summary.cgi?cid=6712209), presented the same pharmacological profile as our derivatives, being active on M14 (AID = 25; source, DTP/NCI) and not on MCF7 cells (AID = 83; source, DTP/NCINCI).

Compounds NSC659611 and NSC671136 fit the pharmacophore models of CCC II, TCT II, TCC I, and TTC II conformers of **8g–i** (Figures 10 and 6SI).

While for NSC659611 only growth inhibition assays are reported (<http://pubchem.ncbi.nlm.nih.gov/assay/assay.cgi?cid=6712209>), several possible molecular targets are indicated for NSC671136, since its biological activity was explored at the molecular level using cell-based assays

Chart 1. Selected 3D Database Search Hits



(pubchem.ncbi.nlm.nih.gov/assay/assay.cgi?cid=383092). Importantly, all reported possible protein targets of NSC671136 are involved in protein–protein interactions regulating DNA transcription. Moreover, the ability of NSC671136 to inhibit MDM2–MDM4 heterodimer formation has also been proven (AID = 489028 and AID = 485346; source, Burnham Center for Chemical Genomics). Noteworthy, the MDM2–MDM4 complex is more efficient in targeting p53 for ubiquitylation and degradation than the MDM2 homodimer, and inhibition of the MDM4–p53 interaction restored p53 function in melanoma cells.²¹ This fascinating hypothesis on the mechanism of action of our derivatives needs deeper investigation to be corroborated. The synthetic feasibility to increase the chemical diversity around the pyrrolic core of our lead compounds will allow the introduction of solubilizing groups to provide analogues more amenable to NMR-based studies, in order to shed light on the

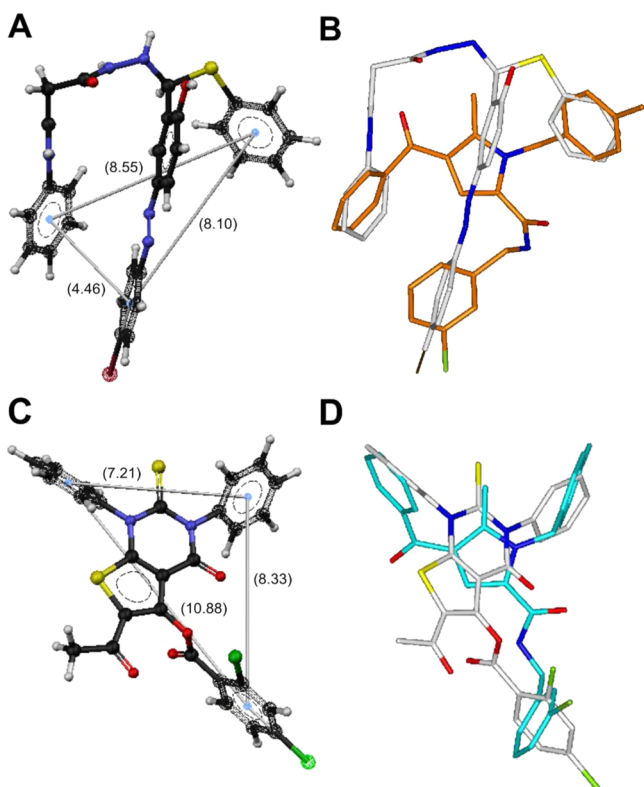


Figure 10. (A) NSC659611 low energy conformer resulting from 3D database pharmacophore search, where matching distances are indicated. (B) Superimposition of CCC II lowest energy conformer of **8i** (carbons, orange) on NSC659611 (carbons, white). (C) NSC671136 low energy conformer resulting from 3D database pharmacophore search, where matching distances are indicated. (D) Superimposition of TCT II lowest energy conformer of **8i** (carbons, cyan) on NSC671136 (carbons, white). Heteroatoms are colored by atom type: O, red; N, blue; S, yellow; Cl, light green.

putative involvement of the p53–MDM2–MDM4 axis in their mechanism of action.

CONCLUSIONS

According to the results obtained through biological investigations, our derivatives **8g–i** interfere with DNA replication, being selectively active against M14 melanoma cells. Our lead **8i** induces a block in the S phase of the cell cycle and an alteration of p53 expression level and nuclear translocation in sensitive cells but not in other cells containing different p53 mutations. SAR and molecular modeling studies strongly support the hypothesis that the ability of our derivatives to mimic LxxLL-like protein recognition motifs is responsible for their antiproliferative activity. Moreover, the results of our 3D database pharmacophore search showed that **8g–i** share pharmacophoric features and cytotoxicity profile with a compound reported to inhibit MDM2–MDM4 complex formation, supporting their hypothesized peptidomimetic ability.

Since protein–protein interactions follow a precise structural code, then understanding the structural basis of this “language” holds the key to developing novel, highly effective, and selective drug candidates. Although further evidence is needed, the selective cytotoxicity toward the M14 cell line suggests a mechanism of action based on the interaction with proteins that are involved in a specific cell signaling pathway, representing a potential benefit in the search for new leads in targeted cancer therapies.

The results of the present study will drive the rational synthesis of new analogues, introducing substituents aimed to optimize both interaction with the hypothesized targets and solubility needed to perform NMR analysis. This approach will allow us to explore the pharmacological potential of our leads as mimetics of protein functional motifs.

EXPERIMENTAL SECTION

Chemistry. Melting points were taken on a Gallenkamp melting point apparatus and are uncorrected. ^1H and ^{13}C NMR spectra were recorded at 300 and 75 MHz, respectively, using a Bruker Avance 300 MHz spectrometer. Splitting patterns are described as singlet (s), doublet (d), triplet (t), quartet (q), quintuplet (qt), and broad (br). Mass spectra were obtained by electrospray ionization (ESIMS) using a Thermo Finnigan LCQ Deca XP Max ion-trap mass spectrometer equipped with Xcalibur software. Chromatographic separations were performed on silica gel (Kieselgel 40, 0.040–0.063 mm, Merck). Reactions and product mixtures were routinely monitored by thin-layer chromatography (TLC) on Merck 0.2 mm precoated silica (60 F254) aluminum sheets, with visualization by irradiation with a UV lamp. All target compounds meet the criteria of >95% purity, as confirmed by combustion analysis performed on a Perkin-Elmer 240 °C elemental analyzer. Yields refer to purified products and are not optimized. All starting materials, reagents, and solvents (reagent grade) were purchased from Sigma-Aldrich and used without further purification.

General Procedure for the Synthesis of Esters 6a–e. Sodium hydroxide (8 mL of a 50% w/v aqueous solution) and tetra-*n*-butylammonium hydroxide (TBAH) (0.1 mL of a 40% w/v aqueous solution) were added to a stirred mixture of **4a** or **4b** (1 mmol) in dichloromethane (8 mL) maintained at 0 °C. After 15 min a solution of selected aryl bromide **5a–d** (1.5 equiv) in dichloromethane (5 mL) was added dropwise. The resulting mixture was allowed to warm to room temperature, stirred in these conditions overnight, and then neutralized with 2 M HCl. The organic phase was washed with brine, dried (Na_2SO_4), filtered, and the solvent was removed under vacuum. The resulting residue was purified by flash column chromatography (SiO_2 , EtOAc/petroleum ether, 40–60 °C, 1:4 v/v).

4-Acetyl-1-benzyl-5-methyl-1H-pyrrole-2-carboxylic Acid Methyl Ester (6a). White solid; mp, 63–65 °C; yield, 96%. ^1H NMR (CDCl_3) δ : 2.48 (s, 3H), 2.55 (s, 3H), 3.81 (s, 3H), 5.68 (s, 2H), 6.96 (d, 2H, J = 7.1 Hz), 7.29 (m, 3H), 7.43 (s, 1H).

4-Benzoyl-1-benzyl-5-methyl-1H-pyrrole-2-carboxylic Acid Methyl Ester (6b). White solid; mp, 93–95 °C; yield, 89%. ^1H NMR (CDCl_3) δ : 2.59 (s, 3H), 3.77 (s, 3H), 5.74 (s, 2H), 7.02 (d, 2H, J = 7.5 Hz), 7.27–7.36 (m, 4H), 7.48–7.58 (m, 3H), 7.84 (d, 2H, J = 7.8 Hz).

4-Benzoyl-1-(4-methyl)benzyl-5-methyl-1H-pyrrole-2-carboxylic Acid Methyl Ester (6c). White solid; mp, 98–100 °C; yield, 76%. ^1H NMR (CDCl_3) δ : 2.34 (s, 3H), 2.59 (s, 3H), 3.77 (s, 3H), 5.69 (s, 2H), 6.92 (d, 2H, J = 7.9 Hz), 7.14 (d, 2H, J = 7.9 Hz), 7.26 (s, 1H), 7.48–7.60 (m, 3H), 7.83 (d, 2H, J = 6.9 Hz).

4-Benzoyl-1-(4-nitro)benzyl-5-methyl-1H-pyrrole-2-carboxylic Acid Methyl Ester (6d). Pale yellow solid; mp, 166–168 °C; yield, 85%. ^1H NMR (CDCl_3) δ : 2.58 (s, 3H), 3.77 (s, 3H), 5.81 (s, 2H), 7.17 (d, 2H, J = 8.4 Hz), 7.30 (s, 1H), 7.49–7.62 (m, 3H), 7.84 (d, 2H, J = 7.1 Hz), 8.22 (d, 2H, J = 8.5 Hz).

4-Benzoyl-1-(4-trifluoromethyl)benzyl-5-methyl-1H-pyrrole-2-carboxylic Acid Methyl Ester (6e). White solid; mp, 115–117 °C; yield, 83%. ^1H NMR (CDCl_3) δ : 2.58 (s, 3H), 3.77 (s, 3H), 5.79 (s, 2H), 7.13 (d, 2H, J = 7.9 Hz), 7.28 (s, 1H), 7.48–7.62 (m, 5H), 7.84 (d, 2H, J = 6.8 Hz).

General Procedure for the Synthesis of Acids 7a–e. To a solution of esters **6a–e** (1 equiv) in methanol (10 mL) was added 2 M NaOH (5 equiv), and the resulting mixture was refluxed until no starting material was detected by TLC. The solvent was removed under reduced pressure. Then the residue was acidified with 2 M HCl (pH \sim 3) and extracted with EtOAc. The organic phase was dried (Na_2SO_4), filtered, and the solvent was removed under vacuum. The resulting residue was purified by column chromatography (SiO_2 , EtOAc/EtOH, 9:1 v/v, as eluent) and recrystallized from ethyl ether/petroleum ether, 40–60 °C.

4-Acetyl-1-benzyl-5-methyl-1H-pyrrole-5-methyl-2-carboxylic Acid (7a). White solid; mp, 187–190 °C; yield, 86%. ^1H NMR (CDCl_3) δ : 2.49 (s, 3H), 2.57 (s, 3H), 5.68 (s, 2H), 6.98 (d, 2H, $J = 7.2$ Hz), 7.30 (m, 3H), 7.57 (s, 1H).

4-Benzoyl-1-benzyl-5-methyl-1H-pyrrole-2-carboxylic Acid (7b). White solid; mp, 175–177 °C; yield, 80%. ^1H NMR ($\text{DMSO}-d_6$) δ : 2.45 (s, 3H), 5.76 (s, 2H), 7.00 (d, 2H, $J = 7.2$ Hz), 7.04 (s, 1H), 7.24–7.37 (m, 3H), 7.51–7.65 (m, 3H), 7.70–7.73 (m, 2H).

4-Benzoyl-1-(4-methyl)benzyl-5-methyl-1H-pyrrole-2-carboxylic Acid (7c). White solid; mp, 173–175 °C; yield, 94%. ^1H NMR (CDCl_3) δ : 2.34 (s, 3H), 2.59 (s, 3H), 5.66 (s, 2H), 6.91 (d, 2H, $J = 8.0$ Hz), 7.13 (d, 2H, $J = 7.9$ Hz), 7.38 (s, 1H), 7.46–7.60 (m, 3H), 7.83 (d, 2H, $J = 6.9$ Hz).

4-Benzoyl-1-(4-nitro)benzyl-5-methyl-1H-pyrrole-2-carboxylic Acid (7d). Pale yellow solid; mp, 216–217 °C; yield, 97%. ^1H NMR ($\text{DMSO}-d_6$) δ : 2.45 (s, 3H), 5.88 (s, 2H), 7.07 (s, 1H), 7.25 (d, 2H, $J = 8.4$ Hz), 7.52–7.66 (m, 3H), 7.74 (d, 2H, $J = 7.1$ Hz), 8.22 (d, 2H, $J = 8.5$ Hz).

4-Benzoyl-1-(4-trifluoromethyl)benzyl-5-methyl-1H-pyrrole-2-carboxylic Acid (7e). White solid; mp, 213–215 °C; yield, 96%. ^1H NMR ($\text{DMSO}-d_6$) δ : 2.46 (s, 3H), 5.84 (s, 2H), 7.10 (s, 1H), 7.21 (d, 2H, $J = 8.0$ Hz), 7.53–7.66 (m, 3H), 7.73 (d, 4H, $J = 6.8$ Hz).

General Procedure for the Synthesis of Compounds 8a–n. To a solution of the acids 7a–e (1 equiv) in DMF (5 mL) were added HOBt (2.5 equiv) and HBTU (2.5 equiv), and the resulting mixture was stirred for 20 min at room temperature. Then *N*-methylmorpholine (NMM) (5 equiv) and the appropriate amine (2.5 equiv) were added, and the resulting mixture was stirred at room temperature overnight. The solvent was removed under reduced pressure, and the resulting residue was taken up in EtOAc and washed successively with 2 M KHSO_4 , saturated solution of NaHCO_3 , and brine. The organic phase was dried (Na_2SO_4), filtered, and concentrated under reduced pressure. The residue was purified by column chromatography (SiO_2 , EtOAc/petroleum ether, 40–60 °C, 1:1 v/v, as eluent) and recrystallized from EtOAc/*n*-hexane to give the title compounds in good yields.

4-Acetyl-1-benzyl-5-methyl-1H-pyrrole-2-carboxylic Acid Benzylamide (8a). White solid. ^1H NMR (CDCl_3) δ : 2.43 (s, 3H), 2.55 (s, 3H), 4.55 (d, 2H, $J = 5.8$ Hz), 5.72 (s, 2H), 6.25 (brs, 1H), 7.00 (m, 3H), 7.25–7.35 (m, 8H). ^{13}C NMR (CDCl_3) δ : 11.68, 28.46, 43.40, 47.89, 113.35, 120.76, 125.08, 126.15, 127.15, 127.26, 127.54, 128.71, 128.74, 137.32, 138.23, 140.50, 161.37, 194.31. ESIMS m/z 347.2 $[\text{M} + \text{H}]^+$.

4-Acetyl-1-benzyl-5-methyl-1H-pyrrole-2-carboxylic Acid Cyclohexylamide (8b). White solid. ^1H NMR (CDCl_3) δ : 1.16–1.25 (m, 2H), 1.32–1.40 (m, 2H), 1.62–1.76 (m, 3H), 1.94 (m, 3H), 2.44 (s, 3H), 2.51 (s, 3H), 3.84 (m, 1H), 5.66 (s, 2H), 5.92 (d, 1H, $J = 7.6$ Hz), 6.94 (s, 1H), 6.99 (d, 2H, $J = 7.1$ Hz), 7.22–7.31 (m, 3H). ^{13}C NMR (CDCl_3) δ : 11.66, 24.87, 25.49, 28.44, 33.15, 47.86, 48.20, 112.85, 120.57, 125.73, 126.13, 127.15, 128.59, 137.32, 140.08, 160.71, 194.40. ESIMS m/z 339.3 $[\text{M} + \text{H}]^+$.

4-Acetyl-1-benzyl-5-methyl-1H-pyrrole-2-carboxylic Acid (3-Phenylpropyl)amide (8c). White solid. ^1H NMR (CDCl_3) δ : 1.92 (qt, 2H, $J = 7.2$ Hz), 2.45 (s, 3H), 2.52 (s, 3H), 2.69 (t, 2H, $J = 7.4$ Hz), 3.41 (q, 2H, $J = 6.7$ Hz), 5.68 (s, 2H), 5.91 (brs, 1H), 6.78 (s, 1H), 6.98 (d, 2H, $J = 7.2$ Hz), 7.20–7.35 (m, 8H). ^{13}C NMR ($\text{DMSO}-d_6$) δ : 11.13, 28.33, 30.92, 32.61, 38.12, 47.66, 114.10, 114.20, 119.89, 124.85, 125.63, 125.98, 126.87, 128.19, 128.45, 137.94, 138.62, 141.69, 160.82, 193.68. ESIMS m/z 375.2 $[\text{M} + \text{H}]^+$.

4-Acetyl-1-benzyl-5-methyl-1H-pyrrole-2-carboxylic Acid 3-Iodobenzylamide (8d). White solid. ^1H NMR (CDCl_3) δ : 2.44 (s, 3H), 2.54 (s, 3H), 4.48 (d, 2H, $J = 5.9$ Hz), 5.70 (s, 2H), 6.22 (brt, 1H, $J = 5.2$ Hz), 6.97–7.08 (m, 3H), 7.19–7.32 (m, 5H), 7.63 (m, 2H). ^{13}C NMR ($\text{DMSO}-d_6$) δ : 11.14, 27.61, 41.18, 46.86, 94.68, 114.71, 120.00, 124.29, 126.00, 126.51, 126.92, 128.49, 130.41, 135.34, 135.64, 137.77, 139.07, 142.38, 160.90, 193.60. ESIMS m/z 473.2 $[\text{M} + \text{H}]^+$.

4-Benzoyl-1-benzyl-5-methyl-1H-pyrrole-2-carboxylic Acid Benzylamide (8e). White solid. ^1H NMR (CDCl_3) δ : 2.55 (s, 3H), 4.51 (d, 2H, $J = 5.8$ Hz), 5.78 (s, 2H), 6.28 (brs, 1H), 6.84 (s, 1H), 7.06 (d, 2H, $J = 6.8$ Hz), 7.20–7.37 (m, 8 Hz), 7.45–7.58 (m, 3H), 7.80 (d, 2H, $J = 7.1$ Hz). ^{13}C NMR (CDCl_3) δ : 11.80, 43.26, 48.06, 114.96, 119.90, 124.88, 126.20, 127.26, 127.43, 127.63, 128.18, 128.64, 128.70, 129.01,

131.51, 137.28, 138.16, 140.00, 141.69, 161.36, 191.96. ESIMS m/z 409.3 $[\text{M} + \text{H}]^+$.

4-Benzoyl-1-benzyl-5-methyl-1H-pyrrole-2-carboxylic Acid Cyclohexylamide (8f). White solid. ^1H NMR (CDCl_3) δ : 1.08–1.22 (m, 3H), 1.31–1.44 (m, 2H), 1.62–1.75 (m, 3H), 1.94 (m, 2H), 2.52 (s, 3H), 3.83 (m, 1H), 5.73 (m, 3H), 6.77 (s, 1H), 7.06 (d, 2H, $J = 7.1$ Hz), 7.24–7.35 (m, 3H), 7.49–7.61 (m, 3H), 7.82 (d, 2H, $J = 7.0$ Hz). ^{13}C NMR (CDCl_3) δ : 11.85, 24.92, 25.52, 33.21, 48.14, 48.29, 114.24, 119.89, 125.70, 126.29, 127.24, 128.22, 128.68, 129.06, 131.49, 137.38, 140.24, 141.31, 160.76, 192.03. ESIMS m/z 401.8 $[\text{M} + \text{H}]^+$.

4-Benzoyl-1-benzyl-5-methyl-1H-pyrrole-2-carboxylic Acid 3-Iodobenzylamide (8g). White solid. ^1H NMR (CDCl_3) δ : 2.55 (s, 3H), 4.46 (d, 2H, $J = 5.8$ Hz), 5.77 (s, 2H), 6.23 (brs, 1H), 6.85 (s, 1H), 7.05 (m, 2H), 7.18 (d, 1H, $J = 7.5$ Hz), 7.29–7.37 (m, 4H), 7.46–7.61 (m, 5H), 7.80 (d, 2H, $J = 7.5$ Hz). ^{13}C NMR ($\text{DMSO}-d_6$) δ : 11.42, 41.06, 46.99, 94.72, 115.82, 118.82, 124.30, 125.96, 126.37, 126.93, 128.17, 128.49, 128.66, 130.49, 131.41, 135.34, 135.50, 137.68, 139.65, 140.80, 142.42, 161.01, 190.74. ESIMS m/z 535.7 $[\text{M} + \text{H}]^+$.

4-Benzoyl-1-benzyl-5-methyl-1H-pyrrole-2-carboxylic Acid 3-Chlorobenzylamide (8h). White solid. ^1H NMR (CDCl_3) δ : 2.54 (s, 1H), 4.50 (d, 2H, $J = 5.6$ Hz), 5.77 (s, 2H), 6.24 (brs, 1H), 6.83 (s, 1H), 7.05 (d, 2H, $J = 6.8$ Hz), 7.20–7.36 (m, 7H), 7.44–7.57 (m, 3H), 7.79 (d, 2H, $J = 6.8$ Hz). ^{13}C NMR (CDCl_3) δ : 11.82, 42.71, 48.12, 115.16, 120.06, 124.67, 125.68, 126.22, 127.37, 127.62, 127.67, 128.22, 128.76, 129.02, 129.93, 131.55, 134.52, 137.23, 140.06, 140.38, 141.85, 161.40, 191.93. ESIMS m/z 443.2 $[\text{M} + \text{H}]^+$.

4-Benzoyl-5-methyl-1-(4-methylbenzyl)-1H-pyrrole-2-carboxylic Acid 3-Chlorobenzylamide (8i). White solid. ^1H NMR (CDCl_3) δ : 2.34 (s, 3H), 2.55 (s, 3H), 4.49 (d, 2H, $J = 5.9$ Hz), 5.71 (s, 2H), 6.19 (brt, 1H, $J = 5.5$ Hz), 6.82 (s, 1H), 6.94 (d, 2H, $J = 7.7$ Hz), 7.08–7.24 (m, 6H), 7.45–7.55 (m, 3H), 7.79 (d, 2H, $J = 7.8$ Hz). ^{13}C NMR (CDCl_3) δ : 11.86, 21.06, 42.74, 47.90, 115.17, 120.02, 124.68, 125.72, 126.21, 127.63, 127.71, 128.21, 129.02, 129.44, 129.91, 131.52, 134.21, 134.54, 137.00, 140.13, 140.42, 141.84, 161.42, 191.93. ESIMS m/z 458.3 $[\text{M} + \text{H}]^+$.

4-Benzoyl-5-methyl-1-(4-nitrobenzyl)-1H-pyrrole-2-carboxylic Acid 3-Chlorobenzylamide (8j). White solid. ^1H NMR (CDCl_3) δ : 2.54 (s, 3H), 4.47 (d, 2H, $J = 6.0$ Hz), 5.85 (s, 2H), 6.25 (brt, 1H, $J = 5.4$ Hz), 6.89 (s, 1H), 7.10 (d, 1H, $J = 5.0$ Hz), 7.19–7.28 (m, 5H), 7.47–7.60 (m, 3H), 7.80 (d, 2H, $J = 7.7$ Hz), 8.20 (d, 2H, $J = 8.2$ Hz). ^{13}C NMR (CDCl_3) δ : 11.59, 42.58, 47.75, 115.35, 120.38, 123.92, 124.34, 125.56, 126.84, 127.48, 127.52, 128.19, 128.92, 129.79, 131.70, 134.37, 139.60, 140.25, 141.26, 144.72, 147.16, 161.07, 191.74. ESIMS m/z 489.1 $[\text{M} + \text{H}]^+$.

4-Benzoyl-5-methyl-1-(4-trifluoromethylbenzyl)-1H-pyrrole-2-carboxylic Acid 3-Chlorobenzylamide (8k). White solid. ^1H NMR (CDCl_3) δ : 2.53 (s, 3H), 4.48 (d, 2H, $J = 5.8$ Hz), 5.82 (s, 2H), 6.32 (brt, 1H, $J = 4.9$ Hz), 6.90 (s, 1H), 7.08–7.29 (m, 6H), 7.46–7.62 (m, 5H), 7.80 (d, 2H, $J = 7.2$ Hz). ^{13}C NMR (CDCl_3) δ : 11.71, 42.72, 47.86, 115.21, 115.24, 120.33, 122.21, 124.44, 125.64, 125.70, 125.75, 125.80, 125.84, 126.44, 127.69, 128.27, 129.01, 129.93, 131.70, 134.55, 140.04 ($J_{\text{C-F}} = 29.5$ Hz), 141.47 ($J_{\text{C-F}} = 17.6$ Hz), 161.19, 191.84. ESIMS m/z 511.7 $[\text{M} + \text{H}]^+$.

4-Benzoyl-1-benzyl-5-methyl-1H-pyrrole-2-carboxylic Acid 3-Nitrobenzylamide (8l). White solid. ^1H NMR (CDCl_3) δ : 2.57 (s, 3H), 4.62 (d, 2H, $J = 6.1$ Hz), 5.77 (s, 2H), 6.34 (brt, 1H, $J = 4.7$ Hz), 6.90 (s, 1H), 7.04 (d, 2H, $J = 6.8$ Hz), 7.30–7.36 (m, 4H), 7.47–7.58 (m, 5H), 7.82 (d, 2H, $J = 6.8$ Hz), 8.13 (m, 1H). ^{13}C NMR (CDCl_3) δ : 11.78, 42.42, 48.10, 115.49, 120.08, 122.12, 122.26, 124.39, 126.12, 127.33, 128.17, 128.72, 128.95, 129.50, 131.56, 133.51, 137.13, 139.91, 140.73, 141.95, 148.33, 161.55, 191.94. ESIMS m/z 454.2 $[\text{M} + \text{H}]^+$.

4-Benzoyl-1-benzyl-5-methyl-1H-pyrrole-2-carboxylic Acid 2,5-Dimethoxybenzylamide (8m). White solid. ^1H NMR (CDCl_3) δ : 2.52 (s, 3H), 3.74 (s, 3H), 3.78 (s, 3H), 4.50 (d, 2H, $J = 6.0$ Hz), 5.76 (s, 2H), 6.45 (brt, 1H, $J = 5.8$ Hz), 6.80 (m, 3H), 6.86 (s, 1H), 7.05 (d, 2H, $J = 7.1$ Hz), 7.25–7.33 (m, 3H), 7.46–7.59 (m, 3H), 7.81 (d, 2H, $J = 6.8$ Hz). ^{13}C NMR (CDCl_3) δ : 11.82, 39.26, 48.11, 55.73, 55.82, 111.41, 113.22, 114.76, 114.79, 115.75, 119.93, 125.30, 126.27, 127.21, 128.13, 128.67, 129.05, 131.46, 137.33, 140.15, 141.46, 151.72, 153.63, 161.27, 191.95. ESIMS m/z 469.6 $[\text{M} + \text{H}]^+$.

4-Benzoyl-1-benzyl-5-methyl-1H-pyrrole-2-carboxylic Acid Biphenyl-2-ylamide (8n). White solid. ^1H NMR (CDCl_3) δ : 2.55 (s, 3H), 5.79 (s, 2H), 6.46 (s, 1H), 7.07 (d, 2H, $J = 7.1$ Hz), 7.17–7.72 (m, 17 H), 8.36 (d, 1H, $J = 8.1$ Hz). ^{13}C NMR (CDCl_3) δ : 11.83, 48.15, 115.48, 119.94, 121.02, 124.11, 124.97, 126.24, 127.36, 128.05, 128.22, 128.44, 128.74, 128.93, 129.04, 129.24, 129.80, 131.42, 132.02, 134.75, 137.11, 137.86, 139.93, 142.52, 159.08, 191.78. ESIMS m/z 471.2 $[\text{M} + \text{H}]^+$.

Cell Culture. Human breast adenocarcinoma MCF7, human melanoma M14, human T cell lymphoblast-like Jurkat, human hepatoma Huh7, and mouse monocyte macrophage Raw 264-7 cell lines were grown at 37 °C in Dulbecco's modified Eagle medium containing 25 mM glucose (DMEM-HG) supplemented with 10% fetal calf serum and 100 units/mL each of penicillin and streptomycin and 2 mmol/L glutamine. At the onset of each experiment, cells were placed in fresh medium and then cultured in the presence of compounds 8a–n (from 0.1 to 100 μM).

Cell Viability Assay. MTT (3-(4,5-dimethylthiazol-2-yl)-2,5-diphenyltetrazolium bromide) assay was used in order to assess the viability of cells to compare the effect of potentially cytotoxic substances with a control condition. Such molecule has a characteristic yellow color and is reduced by mitochondrial enzyme succinate dehydrogenase to a formazan salt, which precipitates as blue/purple crystals. This is a colorimetric assay in which the amount of formazan produced is measured spectrophotometrically and is proportional to the number of viable cells.

To perform the assay, the cells were grown in 96-well plates at 5000 per well and after 24 h were treated with increasing concentrations of compounds 8a–n from 100 nM to 100 μM for 24 and 48 h. At the end of the treatment, the plates were centrifuged at 1200 rpm for 5 min, the medium was aspirated, and an amount of 100 μL of 1 mg/mL MTT was added to each well. The plates were kept at 37 °C for the time necessary for the formation of formazan salt (1–3 h depending on cell type). The solution was then removed from each well, and the formazan crystal within the cells were dissolved with 100 μL of DMSO. Absorption at 550 and 620 nm for each well was assessed by a Multiskan Spectrum Thermo Electron Corporation reader. IC_{50} values were determined using the Prism 4.0 software using nonlinear regression and calculating sigmoidal four-parameter dose–response curves.

Cell viability was also measured by the trypan blue dye exclusion method, which is based on the principle that live cells have intact cell membranes that exclude certain dyes, such as trypan blue, eosin, or propidium, whereas dead cells do not. A cell suspension is mixed with dye and then examined microscopically to determine whether cells take up or exclude the dye. A viable cell will have a clear cytoplasm, whereas a nonviable cell will have a blue cytoplasm.¹³

Exponentially growing cells were plated in 24-well plates. After 24 h of growth, cells were treated with different concentrations of active compounds (5 and 10 μM) dissolved in 0.1% DMSO. Incubation was carried out for different times (24, 48, 72 h). Cells were then exposed to 0.2% trypan blue and counted in a hemocytometer, and the percentage of dead cells was calculated.

Flow Cytometry Analysis. Apoptosis was analyzed by propidium iodide incorporation in permeabilized cells and flow cytometry. Cells (5×10^4) were cultured in 24-wells plates. After 24 h, drugs were added at different doses and cells were recultured for different times (24, 48 h). For apoptosis analysis, permeabilized cells were labeled with propidium iodide (PI) by incubation at 4 °C for 30 min with a solution containing 0.1% sodium citrate, 0.1% Triton X-100, and 50 mg/mL PI (Sigma-Aldrich, St. Louis, MO). The cells were subsequently analyzed by flow cytometry by a FACSCalibur flow cytometer (Becton Dickinson, North Ryde, NSW, Australia).

To evaluate cell cycle distribution, control and treated cells were harvested and nuclei were labeled with PI as described for apoptosis detection and analyzed by flow cytometry. Data from 10 000 events per sample were collected, and the relative percentages of the cells in G0/G1, S, and G2/M phases of the cell cycle were determined using the MODFIT software (Becton Dickinson, San Jose, CA, U.S.). Each determination was repeated three times.

DAPI Staining. M14 cells were cultured on glass coverslips, and after 24 h drugs were added at different doses and cells were recultured for different times (24, 48 h). After 72 h, coverslips were washed in 1 \times PBS and fixed in 3.7% formaldehyde in 1 \times PBS for 30 min at room temperature and for 5 min with 1 \times PBS 0.1 M glycine. For nuclei staining after washing with 1 \times PBS, the coverslips were incubated at room temperature for 20 min with DAPI reagent (Sigma-Aldrich). The coverslips were washed and mounted on microscope slides. Images were collected using an Axiophot microscope (Carl Zeiss MicroImaging) equipped with a Photometrics Sensys camera, and the quantifications of mean fluorescence intensities of nuclei areas were performed by using NIH ImageJ 1.40 software.

Western Blotting Analysis. Cell extracts were lysed in modified RIPA buffer (Tris-HCl, pH 7.4, 10 mM; NaCl 150 mM; EDTA 1 mM; NP40 1%; Na deoxycholic 0.1%; PMSF 1 mM; protease inhibitor cocktail). Equal amounts of proteins were separated by 10–12% SDS-PAGE and blotted on ECL Hybond nitrocellulose membranes (GE Healthcare). Filters were blocked in PBS containing 10% nonfat dry milk and 0.1% Tween-20 and incubated with optimal dilutions of specific antibody for different times depending on the antibodies: cyclin A (Santa Cruz Biotechnology), p53 (Santa Cruz Biotechnology, sc 71819). Anti-rabbit or anti-mouse IgG HRP conjugated (Santa Cruz Biotechnology) were used as secondary antibody. Bands were visualized by autoradiography of ECL reaction (Pierce). Anti- α -tubulin antibody were used as control for equal amounts of proteins loaded on the gel. Level of expression of detected bands was quantified by NIH ImageJ 1.40, and the data obtained after normalization with α -tubulin have been graphically reported.

Nuclear Protein Preparation. To perform the separation of nuclear proteins from cytoplasmic, the initial pellet was resuspended in PTG buffer (10 mM Tris-HCl, pH 7.4, 10% glycerol, 1 mM MgCl_2 , 1 \times protease inhibitors). After 10 min on ice, 0.5% NP40 was added, and after 3 min the mixture was centrifuged at 12 000 rpm at 4 °C for 10 min. The pellet containing nuclei was lysed in RIPA buffer and after 30 min on ice was centrifuged at 14 000 rpm for 20 min at 4 °C. The supernatant, containing nuclear proteins, was recovered. The nuclear lysate was then used in Western blotting analysis.

Statistical Analysis. Statistical analysis was performed with the aid of commercially available software GraphPad Prism4 (GraphPad Software Inc., San Diego, CA). Results are expressed as the mean \pm SEM. One way ANOVA was used to compare groups. The Bonferroni post test was used to compare differences between the groups. $P < 0.05$ was considered as statistically significant.

Protein Expression and Purification. The recombinant human MDM2 (residues 1–118) was obtained from *Escherichia coli* BL21-(DE3) RIL expression system using the vector pET-46Ek/LIC from Novagen. Cells were grown at 37 °C in LB medium and induced for 3 h with 1 mM IPTG at an $\text{OD}_{600\text{nm}}$ of 0.7. After sonication, the inclusion bodies were washed with PBS buffer containing 0.05% Triton X-100, centrifuged at 12000g, and solubilized with 6 M guanidine hydrochloride in 100 mM Tris-HCl, pH 8.0, 1 mM EDTA, and 10 mM DTT. The pH was decreased to 3.5, and then the protein was dialyzed overnight at 4 °C against 4 M guanidine hydrochloride, pH 3.5, including 1 mM EDTA and 10 mM DTT. For MDM2 in vitro refolding, the protein was diluted 1:100 into 10 mM Tris-HCl, pH 7.0, including 1 mM EDTA and 10 mM DTT, by adding the protein in several pulses to the refolding buffer. The refolding was performed overnight at room temperature. Ammonium sulfate was added to the refolded protein at the final concentration of 1.5 M. After 1 h the protein was applied on a Butyl-Sepharose 4 Fast Flow (Amersham). The protein was eluted with 0.1 M Tris-HCl, pH 7.2, supplied with 5 mM DTT. Finally the fractions containing MDM2 were pooled together, concentrated, dialyzed with 50 mM phosphate buffer, 150 mM KCl, 5 mM DTT, and applied to a gel filtration on Sephadex G75. The recombinant human p53 protein (residues 1–312) was overexpressed at 37 °C overnight in *Escherichia coli* BL21(DE3) RIL expression system using the vector pET-46Ek/LIC from Novagen with an N-terminal His-tag. After sonication, the inclusion bodies were washed with PBS buffer containing 0.05% Triton X-100, centrifuged at 12000g, and solubilized with 6 M guanidine hydrochloride in 100 mM Tris-HCl, pH 8.0. The protein was purified under denaturing

conditions using a NiNTA (Qiagen) column, refolded by dilution 1:100 into 10 mM Tris-HCl, pH 7.0, including 0.2 mM ZnCl₂ and 5 mM DTT, by adding the protein in several pulses to the refolding buffer. The refolding was performed overnight at room temperature. Refolded p53 protein was concentrated, dialyzed with 50 mM phosphate buffer, 150 mM KCl, 5 mM DTT, and applied to a gel filtration on Sephadex G75. The p53/MDM2 complex was made by mixing p53 and MDM2 in a ratio of 1:2. The excess of MDM2 was removed by gel filtration on Sephadex G75 and the complex collected concentrated to a final concentration of 0.1 mM and dialyzed into 50 mM phosphate buffer, pH 7.4, 150 mM KCl, 5 mM DTT.

NMR Study of p53–MDM2 Interaction. NMR spectra were acquired at 25 °C on a Varian Unity INOVA 700 MHz spectrometer equipped with a cryoprobe. NMR samples contained 0.1 mM proteins in 50 mM phosphate buffer, 150 mM KCl, pH 7.4, 5 mM DTT, 0.02% NaN₃. Water suppression was carried out by gradient echo.²⁸ NMR data were processed using the Bruker program BioSpin 3.0. For NMR ligand binding experiments, an amount of 300 μ L of the protein sample containing 10% D₂O, at a concentration of about 0.1 mM, and a 10 mM stock solution of compound **8i** or nutlin-3 in DMSO-*d*₆ were used for the experiments. The formal final molar ratio protein/inhibitor was 1:1.

Calculation of **8i Solubility.** Solubility of **8i** was measured adopting the Lipinski et al. method.²⁵ The drug was dissolved in DMSO at 4.6 μ g/ μ L to obtain a 10 mM stock solution. The solution was added a microliter at a time to the phosphate buffer solution (20 mM, 150 mM KCl, pH 7.4) at room temperature (25 °C). The addition of DMSO was spaced 10 min apart. **8i** addition was made. Precipitation was quantified by the absorbance increase due to the light scattering of particulate formed in the cuvette. Increased UV absorbance was measured in the range 500–900 nm to avoid any UV–visible absorption interference in the scattering measurement. (The UV measurements were performed on JASCO-V-530 spectrometer supplied with ETC-S05T temperature controller.) To plot the data in reported in Figure 3SI, two wavelengths were selected, 650 and 850 nm. The precipitation point was identified as the intersect point of the bilinear curve fitted to the plot of absorbance (at each wavelength) vs μ L of DMSO.

Molecular Modeling Studies. Molecular modeling calculations were performed on SGI Origin 200 8XR12000 and E4 Server Twin 2 x Dual Xeon 5520, equipped with two nodes. Each node consisted of 2 x Intel Xeon QuadCore E5520, 2.26 GHz, 36 GB RAM. The molecular modeling graphics were carried out on SGI Octane 2 workstations. The apparent pK_a and solubility values (pH 7.4) of the newly designed pyrrole derivatives **8a–n** were calculated by using the ACD/pK_a DB and ACD/Solubility DB, version 12.00, software (ACD/Labs, Advanced Chemistry Development Inc., Toronto, Canada). All compounds were considered neutral in all calculations performed as a consequence of the estimation of percentage of neutral/ionized forms computed at pH 7.4 (physiological value), using the Handerson–Hasselbalch equation.

Conformational Analysis. The newly designed pyrrole derivatives **8a–n** were built using the Insight 2005 Builder module (Accelrys Software Inc., San Diego, CA). Atomic potentials and charges were assigned using the CFF91 force field.²⁹ The conformational space of compounds was sampled through 200 cycles of simulated annealing ($\epsilon = 1$). In simulated annealing, the temperature is altered in time increments from an initial temperature to a final temperature by adjusting the kinetic energy of the structure (by rescaling the velocities of the atoms). The following protocol was applied: the system was heated up to 1000 K over 2000 fs (time step of 3.0 fs). A temperature of 1000 K was applied to the system for 2000 fs (time step of 3.0 fs) with the aim of surmounting torsional barriers. Successively, the temperature was linearly reduced to 300 K in 1000 fs (time step of 1.0 fs). Resulting conformations were then subjected to molecular mechanics (MM) energy minimization within the Insight 2005 Discover module ($\epsilon = 1$) until the maximum rms derivative was less than 0.001 kcal/Å, using conjugate gradient³⁰ as minimization algorithm. All MM conformers were then subjected to a full geometry optimization by semiempirical calculations, using the quantum mechanical method PM6³¹ in the MOPAC2009 package³² and EF³³ (eigenvector following routine) as geometry optimization algorithm. The GNORM value was set to 0.01. To reach a full geometry optimization, the criterion for terminating

all optimizations was increased by a factor of 100, using the keyword PRECISE. Conformers within 5 kcal/mol from the global minimum ($\Delta E_{\text{GM}} \leq 5$ kcal/mol) were analyzed and grouped into conformational families on the basis of the values of dihedral angles τ_1 , τ_2 , and τ_3 . The centroids of aromatic rings X, Y, and Z were built, and their relative distances were calculated. Conformational families were subclassified into subfamilies on the bases of the obtained sets of pharmacophoric distances, according to the values of τ_4 and τ_5 torsional angles, related to the rotation of X and Y rings. The occurrence rates and ΔE_{GM} range for each conformational subfamily were calculated.

Structural and Bioinformatics Analysis. A structural analysis was performed on X-ray structures containing LxxLL-like and LxxLLxxL-like motifs. In particular, the experimentally determined structures of (i) HDM2 protein in complex with p53 (PDB code 1YCR) and (ii) estrogen receptor β in complex with the nuclear receptor coactivator 5 (Ncoas5; PDB code 2J7X) were downloaded from the Protein Data Bank (PDB, <http://www.rcsb.org/pdb/>). Hydrogens were added to all the structures considering a pH value of 7.2 (Biopolymer Module, Insight 2005). All structures were analyzed using the Insight 2005 Viewer, Biopolymer, and Homology modules (Accelrys, San Diego, CA). The centroids of interacting residues of considered LxxLL-like (*i, i + 3, i + 4*) and LxxLLxxL-like (*i, i + 3, i + 4, i + 7*) motifs were built, and their relative distances were calculated. The resulting values were crossed with the averaged values of **8g–i** pharmacophore distances. In detail, conformational subfamilies of **8g–i** showing a set of pharmacophore distances with at least (i) two values differing less than 1.0 Å and (ii) one value differing less than 1.5 Å from the values of LxxLL-like (*i, i + 3, i + 4*) and/or LxxLLxxL-like (*i, i + 3, i + 4, i + 7*) motif interatomic distances were selected. **8g–i** low energy ($\Delta E_{\text{GM}} \leq 5$ kcal/mol) PM6 conformers belonging to the selected conformational subfamilies were superimposed on LxxLL-like (*i, i + 3, i + 4*) and/or LxxLLxxL-like (*i, i + 3, i + 4, i + 7*) motifs by fitting the centroids of the aromatic rings X, Y, and Z on the centroids of the side chains of the corresponding residues.

Pharmacophore Models Generation and 3D Database Searching. Pharmacophore model building and 3D database searching were performed using CATALYST software package (version 4.6; Accelrys, San Diego, CA). Four fragments, such as three phenyl rings and a halogen atom, were selected as pharmacophore features from the Feature Dictionary. A pharmacophore model was built for each conformational subfamily. Accordingly, the average values of **8g–i** pharmacophoric distances among the three phenyl rings X, Y, and Z were calculated in each conformational subfamily and assigned by using the Set Constraint Tolerance tool by applying a tolerance of ± 0.5 Å (View Hypothesis Workbench; Catalyst). Moreover, in order to assign the distance range between the halogen atom and the Y phenyl ring centroid, the minimum and maximum distance values between any halogen atom attached to a phenyl ring (i.e., F, Cl, Br, and I) and the centroid of this latter were calculated using the quantum mechanical method PM6. All default parameters were used except for the Hydrogen Count in the Set Atom Specification tool. Indeed, in order to specify that the phenyl ring carbons could be bound to any atom, for this parameter the wildcard symbol was used. The Catalyst-generated pharmacophore models were used as query for searching in the chemical 3D databases, and the identified hits were analyzed and classified for their biological activity (MiniBioByte, Maybridge99, Maybridge2001, Sample, NCI2001, Enhanced NCI Database Browser 2.1,³⁴ PubChem²⁷). In order to provide a more accurate search and to increase the number of hits, the BEST flexible search method was used (Max Search Hits, 10 000; flexfit.excessEnergyPerConf, 9.5 kcal). This method is able to change the molecule conformation during execution time. The hits presenting the same pharmacological profile of our derivatives **8g–i** were saved using the Tools/Compare/Fit menu item in the View Compound Workbench (Fast Fit method; Find Best Conf and Max omitted features, –1). Finally, low energy PM6 of the active molecules (**8g–i**) were superimposed on the selected hits by fitting the corresponding pharmacophoric features (i.e., the three phenyl centroids and the halogen atom; Transform/Superimpose command, Viewer, Insight 2005).

■ ASSOCIATED CONTENT

■ Supporting Information

Synthesis of 4-benzoyl-5-methyl-1H-pyrrole-2-carboxylic acid methyl ester (**4b**) and 4-acetyl-5-phenyl-1H-pyrrole-2-carboxylic acid methyl ester (**4c**); 2D ROESY experiments; UV scattering profile caused by a phosphate buffer solution of **8i**; superimposition of CCC I and CCC II conformers of **8i** on the $^{19}\text{F}_{\text{xxLWxxL}}^{26}$ motif present in 1YCR structure; superimposition of conformational enantiomers of **8i** on the $^{19}\text{F}_{\text{xxLWxxL}}^{26}$ motif present in 1YCR structure; NSC659611 low energy conformers resulting from 3D database pharmacophore search and their superimposition on TCC I and TTC II lowest energy conformers; ΔE_{GM} values, torsional angle values, and occurrence rate of conformational subfamilies of **8e**, **8g**, **8h**, **8j**, **8k**, and **8l**; pharmacophoric distances of each conformational subfamily of **8g** and **8h**; distance values used in the generation of pharmacophore models; elemental analysis results for final compounds **8a–n**. This material is available free of charge via the Internet at <http://pubs.acs.org>.

■ AUTHOR INFORMATION

Corresponding Author

*For A.R.: phone, +39089969778; fax, +39089969602; e-mail, aramunno@unisa.it. For S. F.: phone, +39089969793; fax, +39089969602; e-mail, sfranceschelli@unisa.it. For C. F.: phone, +39081678544; fax, +39081678552; e-mail, caterina.fattorusso@unina.it.

Author Contributions

[†]M.P. and A.C. contributed equally to this work.

Notes

The authors declare no competing financial interest.

■ ACKNOWLEDGMENTS

The NMR spectral data were provided by Centro di Servizio Interdipartimentale di Analisi Strumentale (CSIAS), Università degli Studi di Napoli "Federico II". The assistance of the staff is gratefully appreciated. We thank Prof. Tad A. Holak who kindly provided the plasmidic DNA coding for the two p53 and MDM2 constructs. This work was also supported by the PRIN 2009, MIUR (Rome, Italy), (20097YYPRS_002) grant to L.M. Pavone.

■ ABBREVIATIONS USED

SAR, structure–activity relationship; AIDA, antagonist induced dissociation assay; TLC, thin-layer chromatography; MTT, 3-(4,5-dimethylthiazol-2-yl)-2,5-diphenyltetrazolium bromide; MM, molecular mechanics; NMR, nuclear magnetic resonance; HSQC, heteronuclear single quantum correlation spectroscopy

■ REFERENCES

- (1) Garner, A. L.; Janda, K. D. Protein–protein interactions and cancer: targeting the central dogma. *Curr. Top. Med. Chem.* **2011**, *11*, 258–280.
- (2) Jeon, Y. H.; Lee, J. Y.; Kim, S. Chemical modulators working at pharmacological interface of target proteins. *Bioorg. Med. Chem.* **2012**, *20*, 1893–1901.
- (3) Arkin, M. Protein–protein interactions and cancer: small molecules going in for the kill. *Curr. Opin. Chem. Biol.* **2005**, *9*, 317–24.
- (4) Kozakova, D.; Halla, D. R.; Chuanga, G.-Y.; Cencic, R.; Brenke, R.; Grovee, L. E.; Beglova, D.; Pelletier, J.; Whitty, A.; Vajda, S. Structural conservation of druggable hot spots in protein–protein interfaces. *Proc. Nat. Acad. Sci. USA* **2011**, *108*, 13528–13533, S13528/1–S13528/26.
- (5) Wells, J. A.; Mc Clandon, C. L. Reaching for high-hanging fruit in drug discovery at protein–protein interfaces. *Nature* **2007**, *450*, 1001–1009.
- (6) Chi, S.-W.; Lee, S.-H.; Kim, D.-H.; Ahn, M.-J.; Kim, J.-S.; Woo, J.-Y.; Torizawa, T.; Kainosho, M.; Han, K.-H. Structural details on mdm2-p53 interaction. *J. Biol. Chem.* **2005**, *280*, 38795–38802.
- (7) Plevin, M. J.; Mills, M. M.; Ikura, M. The LxxLL motif: a multifunctional binding sequence in transcriptional regulation. *Trends Biochem. Sci.* **2005**, *30*, 66–69.
- (8) Ferlini, C.; Cicchillitti, L.; Raspaglio, G.; Bartollino, S.; Cimitan, S.; Bertucci, C.; Mozzetti, S.; Gallo, D.; Persico, M.; Fattorusso, C.; Campiani, G.; Scambia, G. Paclitaxel directly binds to Bcl-2 and functionally mimics activity of Nur77. *Cancer Res.* **2009**, *69*, OF1–OF9.
- (9) Ferreira, P. M. T.; Maia, H. L. S.; Monteiro, L. S. Synthesis of non-natural amino acids from *N*-(*p*-tolylsulfonyl)- α,β -didehydroamino acid derivatives. *Eur. J. Org. Chem.* **2003**, 2635–2644.
- (10) Ferreira, P. M. T.; Maia, H. L. S.; Monteiro, L. S.; Sacramento, J. High yielding synthesis of dehydroamino acid and dehydropeptide derivatives. *J. Chem. Soc., Perkin Trans. 1* **1999**, 3697–3703.
- (11) Smith, A. B.; Kim, D.-S. A general, convergent strategy for the construction of indolizidine alkaloids: total syntheses of (–)-indolizidine 223AB and alkaloid (–)-205B. *J. Org. Chem.* **2006**, *71*, 2547–2557.
- (12) Toplak, R.; Stanovnik, B.; Svete, J.; Golič Grdadolnik, S. The synthesis of methyl 2-(benzyloxycarbonyl)amino-3-dimethylaminopropenoate. The synthesis of trisubstituted pyrroles, 3-amino-2H-pyran-2-ones, fused 2H-pyran-2-ones and 4H-pyridin-4-ones. *J. Heterocycl. Chem.* **1999**, *36*, 225–235.
- (13) Strober, W. Trypan blue exclusion test of cell viability. *Curr. Protocol. Immunol.* **2001**, *21*, A.3B.1–A.3B.2.
- (14) Woo, A. R.; Poon, Y. C. R. Cyclin dependent kinases and S-phase control in mammalian cells. *Cell Cycle* **2004**, 316–324.
- (15) Frum, R.; Ramamoorthy, M.; Mohanraj, L.; Deb, S.; Deb, S. P. MDM2 controls the timely expression of cyclin A to regulate the cell cycle. *Mol. Cancer Res.* **2009**, *7*, 1253–1267.
- (16) Chi, S.-W.; Lee, S.-H.; Kim, D.-H.; Ahn, M.-J.; Kim, J.-S.; Woo, J.-Y.; Torizawa, T.; Kainosho, M.; Han, K.-H. Structural details on mdm2-p53 interaction. *J. Biol. Chem.* **2004**, *280*, 38795–38802.
- (17) Berglund, H.; Pawitan, Y.; Kato, S.; Ishioka, C.; Soussi, T. Analysis of p53 mutation status in human cancer cell lines. *Cancer Biol. Ther.* **2008**, *7*, 699–708.
- (18) O'Connor, P. M.; Jackman, J.; Bae, I.; Myers, T. G.; Fan, S.; Mutoh, M.; Scudiero, D. A.; Monks, A.; Sausville, E. A.; Weinstein, J. N.; Friend, S.; Fornace, A. J., Jr.; Kohn, K. W. Characterization of the p53 tumor suppressor pathway in cell lines of the National Cancer Institute Anticancer Drug Screen and correlations with the growth-inhibitory potency of 123 anticancer agents. *Cancer Res.* **1997**, *57*, 4285–4300.
- (19) Hsu, I. C.; Tokiwa, T.; Bennett, W.; Metcalf, R. A.; Welsh, J. A.; Sun, T.; Harris, C. C. p53 gene mutation and integrated hepatitis-B viral DNA sequences in human liver cancer cell lines. *Carcinogenesis* **1993**, *14*, 987–992.
- (20) Gomez-Monterrey, I.; Bertamino, A.; Porta, A.; Carotenuto, A.; Musella, S.; Aquino, C.; Granata, I.; Sala, M.; Brancaccio, D.; Picone, D.; Ercole, C.; Stiuso, P.; Campiglia, P.; Grieco, P.; Ianelli, P.; Maresca, B.; Novellino, E. Identification of the spiro(oxindole-3,3'-thiazolidine)-based derivatives as potential p53 activity modulators. *J. Med. Chem.* **2010**, *53*, 8319–8329.
- (21) Gembarska, A.; Luciani, F.; Fedele, C.; Russell, E. A.; Dewaele, M.; Villar, S.; Zwolinska, A.; Haupt, S.; de Lange, J.; Yip, D.; Goydos, J.; Haigh, J. J.; Haupt, Y.; Larue, L.; Jochemsen, A.; Shi, H.; Moriceau, G.; Lo, R. S.; Ghanem, G.; Shackleton, M.; Bernal, F.; Marine, J. C. MDM4 is a key therapeutic target in cutaneous melanoma. *Nat. Med.* **2012**, *18*, 1239–1247.
- (22) D'Silva, L.; Ozdowy, P.; Krajewski, M.; Rothweiler, U.; Singh, M.; Holak, T. A. Monitoring the effects of antagonists on protein–protein interactions with NMR spectroscopy. *J. Am. Chem. Soc.* **2005**, *127*, 13220–13226.
- (23) Krajewski, M.; Rothweiler, U.; D'Silva, L.; Sudipta Majumdar, S.; Klein, C.; Holak, T. A. An NMR-based antagonist induced dissociation assay for targeting the ligand–protein and protein–protein interactions

in competition binding experiments. *J. Med. Chem.* **2007**, *50*, 4382–4387.

(24) Dawson, R.; Mueller, L.; Dehner, A.; Klein, C.; Kessler, H.; Buchner, J. The N-terminal domain of p53 is natively unfolded. *J. Mol. Biol.* **2003**, *332*, 1131–1141.

(25) Lipinski, C. A.; Lombardo, F.; Dominy, B. W.; Feeney, P. J. Experimental and computational approaches to estimate solubility and permeability in drug discovery and development settings. *Adv. Drug Delivery Rev.* **2001**, *46*, 3–26.

(26) Böttger, V.; Böttger, A.; Howard, S. F.; Picksley, S. M.; Chene, P.; Garcia Echeverria, C.; Hochkeppel, H. K.; Lane, D. P. Identification of novel Mdm2 binding peptides by phage display. *Oncogene* **1996**, *13*, 2141–2147.

(27) (a) Bolton, E.; Wang, Y.; Thiessen, P. A.; Bryant, S. H. PubChem: Integrated Platform of Small Molecules and Biological Activities. *Annual Reports in Computational Chemistry*; American Chemical Society: Washington, DC, 2008; Vol. 4, Chapter 12. (b) Wang, Y.; Xiao, J.; Suzek, T. O.; Zhang, J.; Wang, J.; Zhou, Z.; Han, L.; Karapetyan, K.; Dracheva, S.; Shoemaker, B. A.; Bolton, E.; Gindulyte, A.; Bryant, S. H. PubChem's BioAssay Database. *Nucleic Acids Res.* **2012**, *40*, D400–D412 ; <http://pubchem.ncbi.nlm.nih.gov>.

(28) Hwang, T. L.; Shaka, A. J. Water suppression that works. Excitation sculpting using arbitrary wave-forms and pulsed-field gradients. *J. Magn. Reson.* **1995**, *112*, 275–279.

(29) Maple, J. R.; Hwang, M. J.; Stockfisch, T. P.; Dinur, U.; Waldman, M.; Ewig, C. S.; Hagler, A. T. Derivation of class II force fields. I. Methodology and quantum force field for the alkyl function group and alkane molecules. *J. Comput. Chem.* **1994**, *15*, 162–182.

(30) Fletcher, R. Unconstrained Optimization. In *Practical Methods of Optimization*; John Wiley & Sons: New York, 1980; Vol. 1.

(31) Stewart, J. J. P. Optimization of parameters for semiempirical methods V: modification of NDDO approximations and application to 70 elements. *J. Mol. Model.* **2007**, *13*, 1173–1213.

(32) Stewart, J. J. P. MOPAC2009; Stewart Computational Chemistry: Colorado Springs, CO, U.S., 2008; <http://OpenMOPAC.net>.

(33) Baker, J. An algorithm for the location of transition states. *J. Comput. Chem.* **1986**, *7*, 385–395.

(34) Ihlenfeldt, W. D.; Voigt, J. H.; Bienfait, B.; Oellien, F.; Nicklaus, M. C. Enhanced CACTVS browser of the Open NCI Database. *J. Chem. Inf. Comput. Sci.* **2002**, *42*, 46–57 ; <http://cactus.nci.nih.gov/ncidb2.1/>.